

# A comparison of helicopter-borne electromagnetic systems for hydrogeologic studies

Paul A. Bedrosian<sup>1\*</sup>, Cyril Schamper<sup>2</sup> and Esben Auken<sup>3</sup>

<sup>1</sup>Crustal Geophysics and Geochemistry Science Center, U.S. Geological Survey, Denver, CO 80225-0046 USA, <sup>2</sup>Université Pierre et Marie Curie, 75005, Paris, France, and <sup>3</sup>Department of Geoscience, Aarhus University, 8000 Aarhus, Denmark

Received October 2014, revision accepted January 2015

## ABSTRACT

The increased application of airborne electromagnetic surveys to hydrogeological studies is driving a demand for data that can consistently be inverted for accurate subsurface resistivity structure from the near surface to depths of several hundred metres. We present an evaluation of three commercial airborne electromagnetic systems over two test blocks in western Nebraska, USA. The selected test blocks are representative of shallow and deep alluvial aquifer systems with low groundwater salinity and an electrically conductive base of aquifer. The aquifer units show significant lithologic heterogeneity and include both modern and ancient river systems. We compared the various data sets to one another and inverted resistivity models to borehole lithology and to ground geophysical models. We find distinct differences among the airborne electromagnetic systems as regards the spatial resolution of models, the depth of investigation, and the ability to recover near-surface resistivity variations. We further identify systematic biases in some data sets, which we attribute to incomplete or inexact calibration or compensation procedures.

**Key words:** Airborne electromagnetic, Ground water, Inversion.

## 1 INTRODUCTION

Airborne electromagnetic (AEM) methods are widely used within the minerals industry as a primary exploration method, and a wide range of time-domain electromagnetic (TEM) and frequency-domain electromagnetic (FEM) systems have been developed for this purpose. In the last decade, water resource management challenges have prompted the application of AEM methods to basin- or watershed-scale mapping (e.g., Abraham *et al.* 2012; Viezzoli, Munday, and Cooper 2012; Dickinson *et al.* 2010; Green, Brodie, and Munday 2004). Typically, the goals of such studies are to provide constraints on aquifer hydrostratigraphy and the base of aquifer (BOA), including controlling hydrologic channels and flow barriers. As such, it is crucial that AEM resistivity models reflect subsurface resistivity structure as accurately as possible, particularly the position of resistivity boundaries. Understanding the

groundwater quality (e.g., salinity mapping) or the geological structure of aquifers (e.g., the distinction between impermeable clay and porous media such as sand and gravel) further requires accurate estimates of subsurface resistivity and the magnitude of resistivity contrasts. At a minimum, AEM models must be consistent with borehole data and ground geophysical data to extrapolate resistivity models to less constrained areas.

Obtaining a reliable AEM model requires complete system characterization (e.g., geometry, frequencies, waveform, timing, and bandwidth) and accurate modelling (Christiansen, Auken, and Viezzoli 2011). Poor modelling assumptions can lead to egregious errors in the resulting models and, in turn, the hydrologic and geologic interpretations (Viezzoli, Jørgensen, and Sørensen 2013). These effects can include artificial resistive or conductive layers and skewed estimates of saturated-zone resistivity (intimately related to water quality and grain size) or depth to interfaces. Inverting AEM data with an incomplete system description will commonly lead

\*E-mail: pbedrosian@usgs.gov.

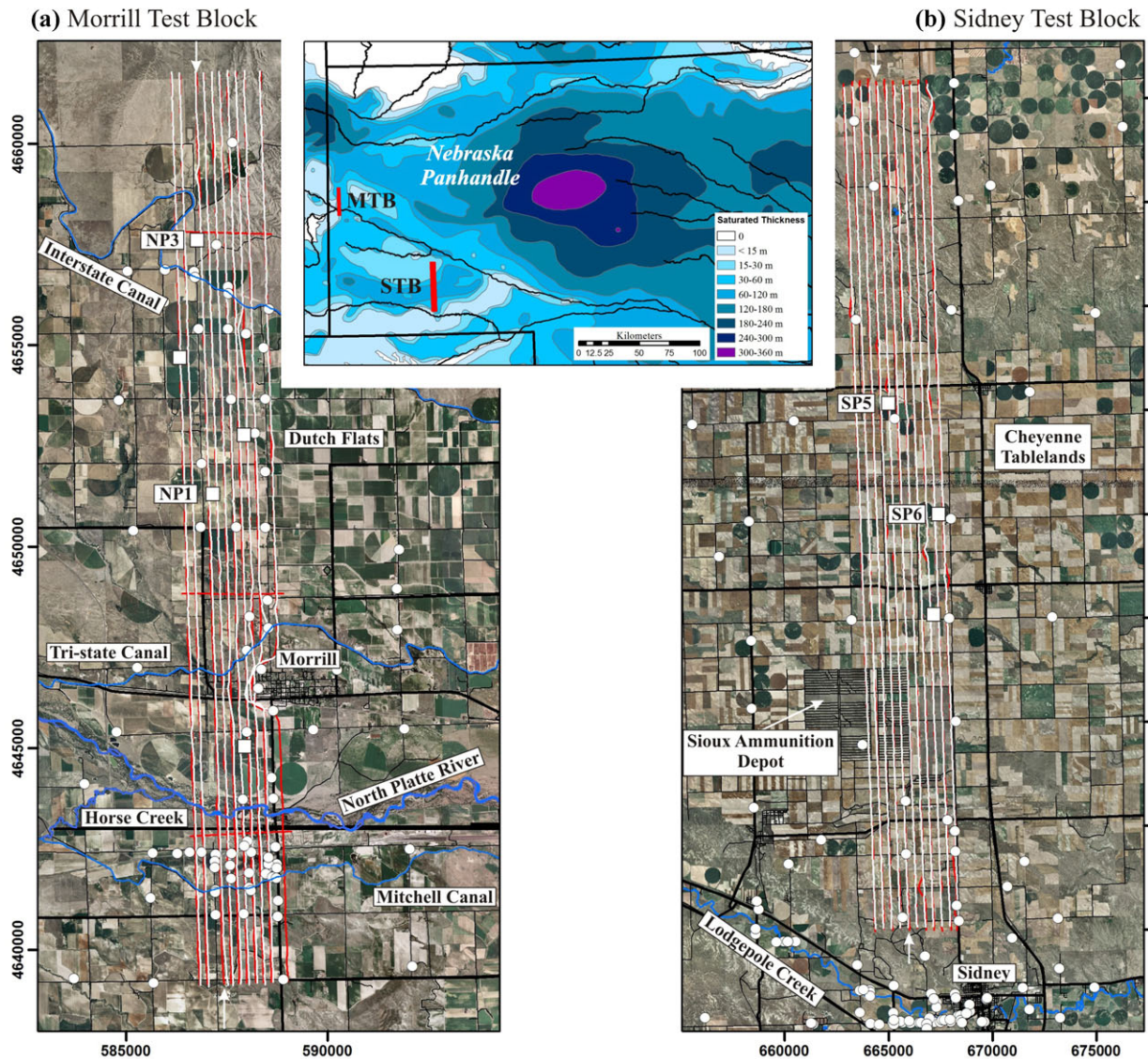


Figure 1 Location map of the (a) Morrill test block (MTB) and the (b) Sidney test block (STB). Inset map shows saturated thickness of the High Plains aquifer within the Nebraska Panhandle (McGuire *et al.* 2012). White and red lines are flight paths from different Airborne Electromagnetic (AEM) systems flown over each test block. White circles indicate boreholes within the survey area; white squares denote locations of Ground-based transient EM (GTEM) soundings. White arrows denote profiles shown in Figs. 5 and 6.

to a realistic, albeit incorrect, resistivity model that fits the data to within measured or estimated data errors. Only rarely does incomplete system specification lead to inverted models totally incompatible with the prior knowledge of the geology or an inability to adequately fit the data.

Comparison studies between different AEM systems have typically focused on mineral exploration, where targets are often highly conductive or very deeply buried. Such studies mainly focus on qualitative analysis in the data space and are primarily concerned with absolute signal levels and target

detection (Smith *et al.* 2011; Cunion 2009; Hodges and Beattie 2007; Smith, Annan, and McGowan 2001). Within a hydrologic context, the area of interest is most often within the first 100 m–300 m, is very often in the first 50 m, and is characterized by significantly smaller resistivity contrasts than in mineral exploration. Furthermore, while target detection and plate modelling may be sufficient for mineral exploration in many situations, the interpretation of AEM data for hydrologic applications is always predicated upon resistivity–depth images produced via an inversion process.

Outside of mineral exploration, few system comparison studies exist. Davis and Groom (2010) present a comparison of several airborne and ground TEM (GTEM) systems over a thick sedimentary sequence but focus on system calibration and sensitivity studies. Steuer, Siemon, and Auken (2009) present the closest analogue to the present paper, where they compare DIGHEM and SkyTEM data in a buried valley setting in Northern Germany. They examine AEM inversion models for each system as regards structure delineation, depth of investigation (DOI), and correlation with ground-based resistivity models. We expand upon this approach and consider three AEM systems within a different hydrologic setting. We delve into the details of data processing and inversion, present a statistical comparison of the various systems as related to model resolution and model correlation, and carry out a more extensive comparison of AEM models and borehole lithology.

We present a case study in which three of the most widely used helicopter-borne AEM systems (RESOLVE, SkyTEM 304, and AeroTEM IV) were flown with identical survey specifications over two test blocks (235 line-kms and 444 line-kms) in western Nebraska, USA. A prototype of the VTEM Plus system from Geotech Ltd. was additionally flown over one of the test blocks but is not presented here. The two test blocks, near Morrill and Sidney, Nebraska, are characteristic of shallow and deep alluvial aquifer systems, respectively, within the High Plains aquifer and, more generally, of alluvial systems worldwide. We modelled and inverted each data set taking into account each instrument's specific system response, waveform, timing, geometry, and auxiliary navigational data. System noise levels were established, and regions contaminated by cultural noise were culled in a consistent and systematic fashion. While we made every attempt to model each system as accurately as possible based on contractor specifications, we did not attempt to calibrate any of the data sets to account for unknown or undocumented shifts or biases; only calibration provided by the contractors was considered. Identifying and correcting calibration problems are beyond the scope of this paper; we point the reader to studies by Podgorski *et al.* (2013); Minsley *et al.* (2012); Ley-Cooper and Macnae (2007); and Deszcz-Pan, Fitterman, and Labson (1998). Data sets were inverted using a consistent framework and are presented with a common metric for DOI (Christiansen and Auken 2012). We examine the correlation of the resulting models with borehole lithology and ground-based geophysical data. Within a hydrogeologic context, we demonstrate the ability of each system to resolve particular structures within the test areas,

to define internal aquifer stratigraphy, and to constrain the BOA.

## 2 HYDROGEOLOGIC SETTING

The study areas are located within the western Nebraska Panhandle along the North Platte River Valley (NPRV) and within the Cheyenne Tablelands (inset in Fig. 1). This region falls within the High Plains aquifer system, one of the largest aquifer systems in the world. It spans eight states, and saturated thicknesses can exceed 300 m (Fischer, Kollasch, and McGuire 2000). In western Nebraska, the High Plains aquifer includes hydrologically connected units of Tertiary and Quaternary ages, including the Miocene- and Oligocene-age Arikaree Group, the Miocene- and Ogallala-age Formation, and the Quaternary-age alluvial deposits (Table 1). The Oligocene-age Brule Formation forms the BOA throughout much of the study area.

The relatively impermeable Brule Formation is a massive siltstone composed primarily of eolian silt, with some alluvial deposits. Deposits of volcanic ash derived from eruptions in the western United States make up two-thirds of its volume. Overlying the Brule Formation is the Arikaree Group, a fine-grained sandstone with localized beds of volcanic ash, silty sand, and sandy clay. Where present, the Arikaree Group is considered part of the High Plains aquifer system; however, it does not yield large quantities of water to wells (Gutentag *et al.* 1984). The Miocene Ogallala Group is the principal geologic unit in the High Plains aquifer system and can reach a thickness in excess of 300 m beneath the Sandhills of central Nebraska (McGuire, Lund, and Densmore 2012; Diffendal 1991). The Ogallala Group was deposited by aggrading streams that filled paleovalleys eroded into older rocks (Swinehart *et al.* 1985). An unconformity of at least 1.5 million years separates the Ogallala Group from the Pliocene Broadwater and the Pleistocene Long Pine formations (Swinehart and Diffendal 1998). These sediments are unevenly deposited and preserved but contain coarse sand and gravel separated by finer grained deposits. They are considered to be in hydrologic connection with the underlying Ogallala Group. Ground and airborne geophysical surveys within western and central Nebraska support a resistivity stratigraphy in which the BOA (Brule Formation) averages 10  $\Omega\text{m}$ –15  $\Omega\text{m}$ , the Ogallala and Arikaree groups span a range of 20  $\Omega\text{m}$ –100  $\Omega\text{m}$ , and Pliocene and Pleistocene sand and gravel deposits are typically >100  $\Omega\text{m}$  (Abraham *et al.* 2012; Hobza, Bedrosian, and Bloss 2012). Groundwater salinity is low within the unconfined aquifer.

**Table 1** Stratigraphic section for western Nebraska, including hydrologic and geophysical characteristics. Resistivity estimates from Hobza, Bedrosian and Bloss (2012). Thickness estimates are from Steele, Sibray and Quandt (2007) and Verstraeten *et al.* (2001). Thick horizontal lines indicate regional unconformities.

Period	Epoch	Stratigraphy		Lithology	Hydrogeologic unit	Resistivity ( $\Omega\text{m}$ )	Thickness (MTB)	Thickness (STB)
Quaternary	Holocene	Alluvium & eolian deposits		gravel, sand, silt & clay	High Plains aquifer	< 50	variable, < 50 m typically	variable, < 10 m typically
	Pleistocene	Long Pine Formation & undifferentiated alluvial & eolian deposits				> 100	variable, < 30 m typically	variable, < 10 m typically
Tertiary	Pliocene	Broadwater Formation		gravel & sand		20-100	---	variable, up to 200 m
	Miocene	Ogallala Group		gravel, sand, silt & clay			< 30 m	---
		Arikaree Group		very fine to fine-grained sandstone				
	Oligocene	White River Group	Brule Formation	siltstone & mudstone	local confining unit with discontinuous high-permeability lenses & fractures	10-15	< 200 m	< 200 m
				sand & gravel		30-?		
	Eocene	White River Group	Chadron Formation	mudstone	local confining unit with discontinuous high-permeability lenses	10	< 30 m	?
sandstone				30-?		> 30 m, locally	?	
Cretaceous	Late	Pierre Shale		shale	regional confining unit	5	< 150 m	< 150 m

## 2.1 Morrill test block (MTB)

The Morrill test block (MTB) encompasses the NPRV and the Dutch Flats region to the north of it (Fig. 1). At the northern edge of the MTB, coarse sand and gravel deposits, most likely Pliocene and Pleistocene in age, are exposed in hill slopes. The MTB is representative of a shallow alluvial aquifer system and includes broad channels incised into the Brule Formation by both the ancestral and modern-day North Platte River systems. The MTB is 40 km<sup>2</sup> in area and oriented north/south; it consists of ten 22-km-long lines with a nominal line spacing of 200 m. Surface elevation ranges from 1210 m above sea level (asl) within the NPRV to 1340 m asl along a topographic ridge along the north end of the survey block. A network of rural roads and powerlines is present within the survey area, as well as the town of Morrill. Borehole data (Conservation and Survey Division of the University of Nebraska-Lincoln) within this block include 64 holes, the majority of which penetrated

the BOA at depths ranging from a few metres to over 100 m. Geophysical data within the MTB include ground-based TEM soundings at 5 locations. The hydrostratigraphy and groundwater systems within the MTB are described by Cannia, Woodward, and Cast (2006) and Verstraeten *et al.* (2001).

## 2.2 Sidney test block (STB)

The Sidney test block (STB) spans the Cheyenne Tablelands between the NPRV and Lodgepole Creek, a tributary to the South Platte River (Fig. 1). It is representative of a deep alluvial aquifer system and progressively shallows to the North. Sand and gravel paleochannels are incised at various depths within the Brule Formation. Discontinuous sand and gravel lenses, typically less than 10 m thick, are also present within the Brule Formation (Steele, Sibray, and Quandt 2007). The STB is 165 km<sup>2</sup> in area and is oriented north/south; it consists of eleven 40-km-long lines with a nominal line spacing of 400 m.

**Table 2** Technical specifications of AEM systems flown over the Morrill and Sidney test areas.

System designation	STEM	DTEM	FEM
Trade names	AeroTEM IV	SkyTEM 304	RESOLVE
Company	Aeroquest Ltd.	SkyTEM surveys	Fugro
Type	time domain, rigid frame central loop receiver single moment	time domain, rigid frame null-coupled Z receiver dual moment	frequency-domain 5 coplanar freqs, 7.9 m separation 1 coaxial freq, 9.0 m separation
Waveform	bipolar triangular	bipolar square wave	continuous
Base frequency (Hz)	90	30	–
Spectrum <sup>a</sup>	58 $\mu$ s – 3.2 ms	3 $\mu$ s – 7.1ms	400 Hz – 130kHz
N turns	5	1 (LM), 4 (HM)	
Current (peak, A)	397	10 (LM), 100 (HM)	100
Area	115	314	–
Moment (Am <sup>2</sup> )	237,000	3,000 (LM), 120,000 (HM)	310 (400 Hz) –18 (130 kHz)
Average sensor height (m)	48 +/- 8	32 +/- 5	36 +/- 6
Positioning (helicopter)	GPS – on mag Radar	GPS Radar	GPS Radar
Positioning (frame)	–	GPS, Laser (2) Inclinometer (2)	GPS Laser

<sup>a</sup>The zero timing is defined as the end of the ramp

Surface elevation ranges from 1150 m asl at the north end of the STB to 1330 m asl in the Cheyenne Tablelands. A network of roads and powerlines crosses the STB in addition to a major power transmission line and pipeline. The Sioux Army Depot, a World War II-era ammunition depot consisting of hundreds of metal-reinforced concrete bunkers, also lies within the STB. Ground control is more limited within the STB, with only 17 boreholes and 3 ground-based TEM soundings. Nearly 500 deep oil and gas wells, however, have been drilled within the STB (Nebraska Oil and Gas Conservation Commission). While these wells provide constraints on the Cretaceous and older stratigraphy (Table 1), they rarely provide information on the overlying Tertiary and Quaternary sections.

### 3 DATA PROCESSING AND INVERSION

Five surveys were flown in total between 2008 and 2012. A prototype of the VTEM Plus system from Geotech Ltd. was additionally flown over the STB, but the data were not made available for this paper. We present details of the individual systems in the order in which they were flown. All flight heights, regardless of system, fluctuated during the survey due to topography and man-made obstacles. As higher flight altitudes result in a lower signal-to-noise ratio and in a loss of lateral and vertical resolution, the AEM systems were always flown as close to the ground as possible. The average

sensor height varied from system to system, ranging between 32 m and 48 m above land surface. In the descriptions that follow, we focus on parameters relevant to our modelling efforts; more complete technical specifications can be found in Table 2. We note that, in what follows, all gate times for TEM systems are referenced to a time-zero point at the end of the current turn-off.

#### 3.1 Frequency-domain helicopter-borne EM system (FEM)

The RESOLVE system (e.g., Brodie and Sambridge 2006; Brodie, Green, and Munday 2004) is the FEM system considered. Given its high-frequency content and compact footprint (Reid and Vrbancich 2004), this FEM system is expected to offer better near-surface resolution, both in vertical and horizontal directions, in comparison with the TEM systems flown above the two blocks. Additionally, FEM systems typically have a smaller DOI than TEM systems, usually not exceeding 70 m–100 m. TEM systems, in contrast, can often investigate more than 300 m provided that the overburden resistivity is not too low. This difference in DOI is due to practical limitations in airborne FEM systems on both the transmitter-to-receiver coil separation, which cannot be considerably increased without degrading flight stability, and the transmitter moment, which cannot be increased without affecting removal of the large primary magnetic field. The FEM system has a fixed-geometry frame where transmitter and receiver coils are

aligned in the flight direction. It records six different frequencies from about 400 Hz to 130 kHz: five horizontal coplanar frequencies and one vertical coaxial frequency (Fig. 2a). The waveform is a continuous sine wave; hence, the recorded data are the in-phase and out-of-phase, or quadrature, components of the secondary magnetic field at each discrete frequency (Fig. 2a). The data are expressed in parts per million (ppm) in relation to the primary field measured at the receiver coil (i.e., the electromagnetic (EM) field that diffuses directly from the transmitter to the receiver coil in the air). The FEM system was flown over the MTB in June 2008 (Smith *et al.* 2009; Fugro Airborne Surveys 2008) and over the STB in September 2009 (Abraham *et al.* 2012; Smith *et al.* 2010; Fugro Airborne Surveys 2009).

### 3.2 Single-moment transient EM system (STEM)

The AeroTEM system (here, version IV) is a rigid-frame central-loop TEM system (e.g., Bedrosian, Ball, and Bloss 2014; Balch, Boyko, and Paterson 2003). It employs a bipolar triangular waveform with a repetition frequency of 90 Hz to eliminate harmonics associated with the 60-Hz electrical network. In addition to off-time data, on-time gates are measured during the downstroke of the current waveform. These gates are qualitatively used to detect highly conductive targets sometimes encountered in mineral exploration but cannot be incorporated within standard inversion programs due to the strong primary field, which cannot be completely removed. We found it necessary to disregard the first two off-time gates as a pervasive non-physical “kink” is observed in the decay curves (Fig. 2b, prior to 100  $\mu$ s), which is likely due to the proximity of the turn-off ramp. The latest gate recorded by this system is 3.2 ms. With a transmitter area of 115 m<sup>2</sup> but with a transmitter moment of 237,000 Am<sup>2</sup> (Table 2), the STEM system has a higher moment than the dual-moment SkyTEM 304 system. Another version of the system, AeroTEM HD, provides a higher moment of 1,000,000 Am<sup>2</sup> for deeper investigations. The STEM system was flown over the MTB in November 2008 (Aeroquest Surveys 2009).

### 3.3 Dual-moment transient EM system (DTEM)

The SkyTEM system (here, version 304) is a rigid-frame dual-moment TEM system developed over the past 10 years (Sørensen and Auken 2004). In contrast to the other TEM systems, the SkyTEM system has the receiver coil positioned slightly behind the transmitter wire in a “null” position, where the intensity of the primary field is minimized (Schamper, Auken, and Sørensen 2014). The SkyTEM system was ini-

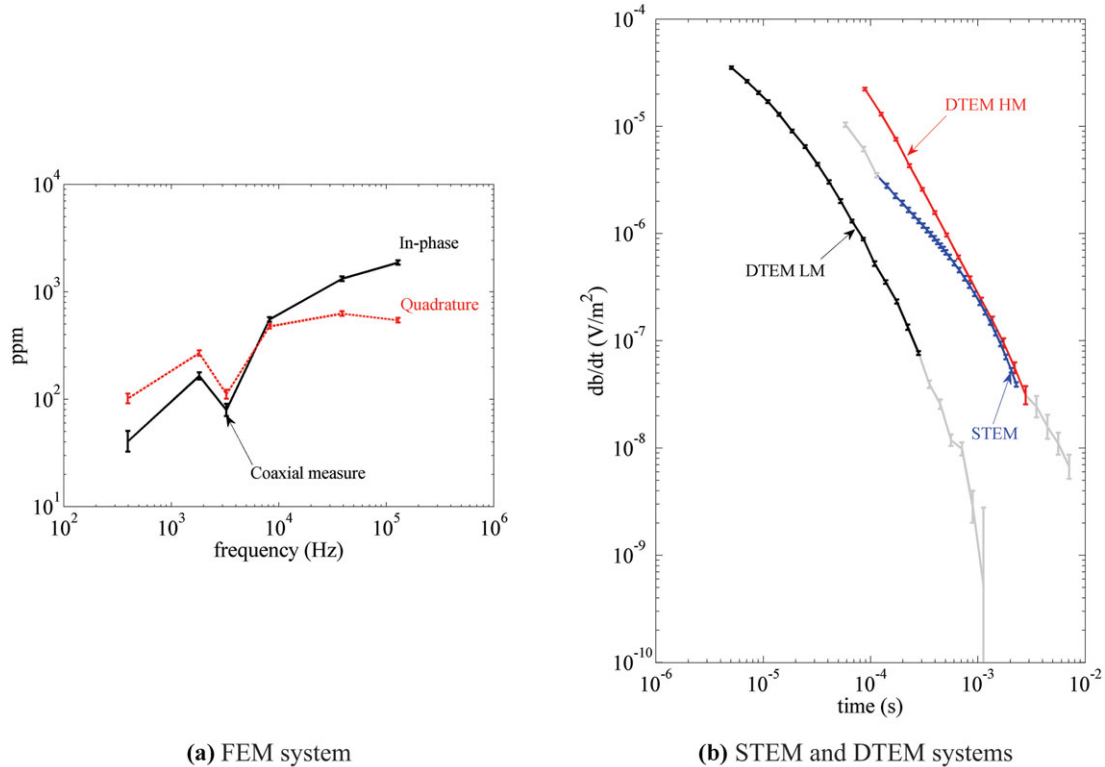
tially designed for groundwater mapping, and to reach this goal, it employs two transmitter moments with different currents and different numbers of transmitter wire turns (Fig. 2b, black and red curves). The low current, or low-moment (LM) mode, with a moment of 3000 Am<sup>2</sup>, is used to record early-time data, which constrain near-surface information, whereas the high current, or high-moment (HM) mode, with a moment of 120,000 Am<sup>2</sup>, improves the signal-to-noise ratio at late times. The DTEM system flown for this study (SkyTEM 304) has a transmitter area of 314 m<sup>2</sup> and is intermediate between the SkyTEM 101 system, used for near-surface applications, and the SkyTEM 508, designed for deeper investigations. The DTEM system records time gates from 3  $\mu$ s to 7 ms. The gates interpreted in the STB survey fall between 5  $\mu$ s and 4.5 ms, with the latest recorded gates being too noisy to be used and the gates before 5  $\mu$ s contaminated by residual primary field. The correction of early-time data for the residual primary field is done in more recent SkyTEM surveys and permits the use of data as early as 2  $\mu$ s–3  $\mu$ s, thus improving near-surface resolution (Schamper, Auken, and Sørensen, 2014). The LM DTEM data provide earlier off-time data compared with the STEM system. The DTEM system was flown over the STB in June 2010 (Aarhus Geophysics 2010; SkyTEM Surveys Aps 2010).

### 3.4 Ground-based transient EM (GTEM) soundings

Eight GTEM soundings were acquired within the MTB and STB using a Geonics ProTEM 47 system (Fig. 1, white squares). This system was calibrated prior to data collection at an established test site (Foged *et al.* 2013). All data were collected using a 100-m square transmitter loop and an air-coil receiver in both central- and out-of-loop configurations. Measured data were collected using low- and high-power transmitters with moments of 20,000 Am<sup>2</sup> and 200,000 Am<sup>2</sup>, respectively. The data span a time range from 9  $\mu$ s to greater than 10 ms after the end of the current turn-off. Data were processed and inverted using the SiTEM/Semdi software packages (Auken and Nebel 2001). All soundings were determined to have a DOI of at least 400 m, and more typically 500 m, using the method of Christiansen and Auken (2012). Additional details of the acquisition and processing of these soundings can be found in Abraham *et al.* (2012).

### 3.5 Data pre-processing

As delivered, the four data sets from the three AEM systems reflect different levels of pre-processing. The data from the



(a) FEM system

(b) STEM and DTEM systems

**Figure 2** Characteristic response for (a) the Frequency-domain Electromagnetic (FEM) system and (b) the Single-moment transient EM system (STEM) and Dual-moment transient EM system (DTEM) systems. Error bars are calculated as described in the text and are consistent with those applied during subsequent inversion. Time gates in grey have been deactivated due to low-signal-to-noise ratio at late times or due to the presence of primary field at early times. These gates are not included within the inversion.

FEM system can be considered “averaged” data, as stacking and along-line smoothing filters have already been applied, resulting in data with high-signal-to-noise ratio and little or no indication of scatter in the low-frequency data. The STEM and DTEM systems have smoothing filters applied to the data sets, but to a lesser extent, so that supplementary stacking is required in a post-processing step.

The pre-processing parameters obtained from the different companies are summarized in Table 3. Note that FEM data are very dense spatially, about one sounding every 3 m, much smaller than the footprint of any AEM system (Reid and Vrbancich 2004). While STEM data are also delivered with a 2-m to 3-m sounding spacing, additional stacking is required at late times to improve the signal-to-noise ratio, resulting in a smoothed sounding density of  $\sim 15$  m. This is similar to the sounding density of pre-stacked DTEM data (15 m). To homogenize all data sets to the same data density, FEM data were decimated to a sounding spacing of 15 m, which is close to the best resolution this FEM system can reach in practice (without loss in S/N ratio as data are already pre-stacked). This is comparable to what is obtained from STEM and DTEM data

where final sounding spacing after stacking is also about 15 m (Table 3).

### 3.6 Data post-processing

Prior to inverting AEM data, cultural noise, in which man-made objects couple to the AEM system, must be identified and removed (Viezzoli, Jorgensen, and Sorensen, 2013). Knowledge of the locations of potential sources of coupling helps in this processing, and a geographic information system-based approach is used to examine the location of suspect data in relation, for example, to powerlines and pipelines. We decided to apply a conservative culling procedure in which we removed entire soundings even if only the late gates or low frequencies appear affected. In this manner, we greatly limit the risk of remaining couplings and therefore of biased interpretation due to non-geological conductive anomalies.

While an examination of the data from the MTB did not reveal significant cultural noise (Fig. 3 shows a representative sample), the Sidney block data are heavily contaminated by cultural noise (Fig. 4). A prominent power transmission line

Table 3 Pre- and post-processing parameters applied to the individual data sets.

	STEM	DTEM	FEM
Pre-processing			
Number of gates/frequencies	36	26/34 <sup>a</sup>	6
Gate type	Boxcar	Boxcar	–
Filter type	Boxcar	Boxcar	N.A.
Filter width	36 points	120/64 <sup>a</sup>	N.A.
Overlap	50%	0%	N.A.
Smoothing filter type	Hanning	–	N.A.
Smoothing filter width (nb. of soundings)	19	–	N.A.
Smoothing filter width (m)	15 m	–	N.A.
Sounding spacing as delivered	0.1 s/~2 m <sup>c</sup>	0.6 s/~15 m <sup>c</sup>	0.1 s / ~3.2 m <sup>b</sup>
Post-processing			
Manual culling of the couplings	Yes	Yes	Yes <sup>d</sup>
Stacking width	10 $\mu$ s < t < 100 $\mu$ s: 4 s 100 $\mu$ s < t < 1 ms: 10 s t > 1ms: 30s	t < 10 $\mu$ s: 2 s 10 $\mu$ s < t < 100 $\mu$ s: 4 s 100 $\mu$ s < t < 1 ms: 10 s t > 1 ms: 30 s	–
Final sounding spacing	0.6 s/~13 m	0.6 s/~15 m	0.4 s / ~15 m

<sup>a</sup>LM and HM settings

<sup>b</sup>The average sounding distance is estimated according to the cruise speed of this specific survey

<sup>c</sup>These numbers are for “almost raw” data; FEM data are already averaged and smoothed when delivered

<sup>d</sup>The culling of these data has been done after the stacking already made and delivered by the contractors; raw data were not available

runs northwest to southeast through the survey area (Fig. 4, box 2), whereas numerous smaller powerlines cross the test block and are typically aligned along roads (Fig. 4, boxes 3 and 4). In addition, a pipeline crosses the test block. Finally, metal-reinforced ammunition bunkers of the Sioux Ammunition Depot give rise to regular-spaced spikes in the measured data (Fig. 4, box 1). Culling of the coupled data is carried out *prior* to the post-processing stack step, as detection of coupled data is much easier and removal of them is more efficient, when the data have not been stacked (which is a smoothing operation). The post-processing stack is not applied to FEM data, which are simply decimated to standardize data density. For STEM and DTEM data, trapezoidal stacking filters have been applied to improve the signal-to-noise ratio at the latest time gates (Figs. 3a and 4a). The stacking width of these filters increases with time so that almost no stacking is applied to the earliest time gates where the ground response is sufficiently strong. The time-dependent stacking widths are detailed in Table 3.

### 3.7 Modelling and inversion

Estimation of background noise levels for each system must be carried out prior to inversion. A standard deviation

is applied to each gate or frequency such that data with large errors have very little weight during the inversion process. Inverting data with artificially small errors tends to produce rough model sections and may result in artificial conductive anomalies at depth. In contrast, inverting data with artificially large errors mutes model structure, producing heavily smoothed model sections that do not capture the variability in the measured data.

Data errors for the various systems were either statistically determined, in cases where “raw” data were delivered (STEM and DTEM systems), or based upon a noise model, where data were filtered and stacked prior to delivery (FEM system), thus prohibiting a meaningful statistical error estimate. In all cases, a minimum 5% relative error (error floor) was applied. For the STEM and DTEM data, statistically determined errors were estimated for each gate from the trapezoidal stacking filters specified in Table 3. The application of the above data errors is illustrated in Fig. 2 for a sample sounding from each system.

Error estimation for the FEM data is based upon a noise model incorporating relative and absolute error terms, following the approach of Finn, Deszcz-Pan, and Bedrosian (2012), where the variance associated with each data point is defined through error propagation as the sum of the squared

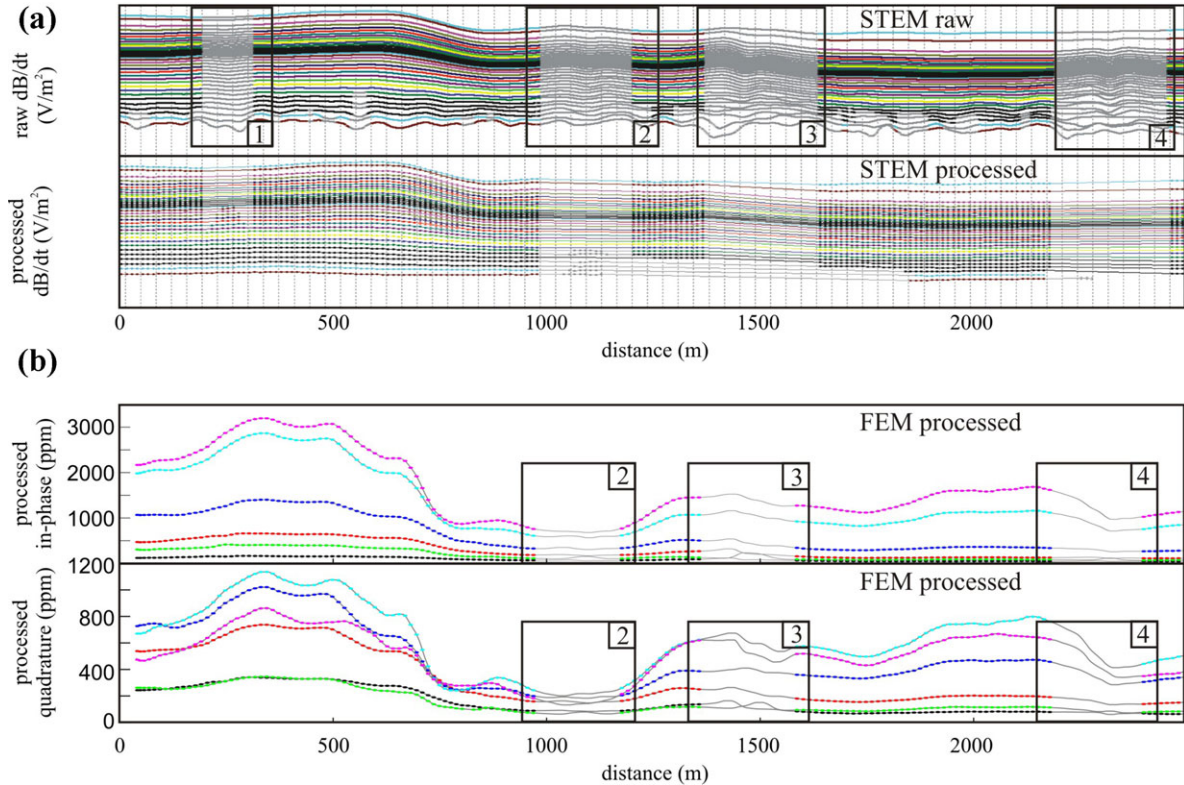


**Figure 3** Spatially collocated data segments within the Morrill block from (a) STEM and (b) FEM systems. Each time window corresponds to roughly 3 minutes of measured data. Each curve represents a particular (a) time gate or (b) frequency. Average STEM data correspond to the result of the post-processing stack (Table 3). Numbered boxes indicate where cultural noise has been identified in the data and discarded from the data set.

errors. The absolute and relative errors were set to 10 ppm and 5%, respectively, and collectively account for stochastic noise, inaccurate drift correction, calibration errors, and variations in system geometry.

All data sets were treated as uniformly as possible with regard to data processing, inversion, and the presentation of results. Our analysis, however, was carried out on the data as delivered, and therefore, individual data sets reflect differing degrees and approaches to primary field removal (sometimes termed compensation), correction for non-zero response at high altitude (sometimes termed bias correction), filtering, and levelling. We have inverted all data using the spatially constrained inversion (SCI) of Viezzoli *et al.* (2008) structured about the AarhusInv inversion code (Auken *et al.* 2005; Auken and Christiansen 2004). The same inversion parameters were applied to all data sets (Table 4). System geometry, filters, waveforms, frequencies, and time gates were modelled as accurately as possible (Christiansen *et al.* 2011) given the contractor specifications.

The SCI approach applies vertical and horizontal regularization as a series of constraints, which favour resistivity models that vary smoothly both laterally and with depth throughout the survey area. The strength given to these constraints is partly defined based on experience, keeping in mind that the constraints must not be so strong as to prevent fitting of the data. Lateral constraints help preserve continuity between nearby soundings and are adjusted so as to have a real impact only on parameters that are poorly defined by the data, such as deep layers near or below the DOI. The DOI varies as a function of model resistivity, system altitude, and the latest time gate or lowest frequency used. We compute a sensitivity-based DOI metric at each sounding location once the resistivity models have been estimated during the inversion using the approach of Christiansen and Auken (2012). This metric is best viewed as a relative indicator of how DOI varies spatially within each test block and between different systems at a fixed location. The DOI helps avoid over-interpretation of the resistivity–depth images,

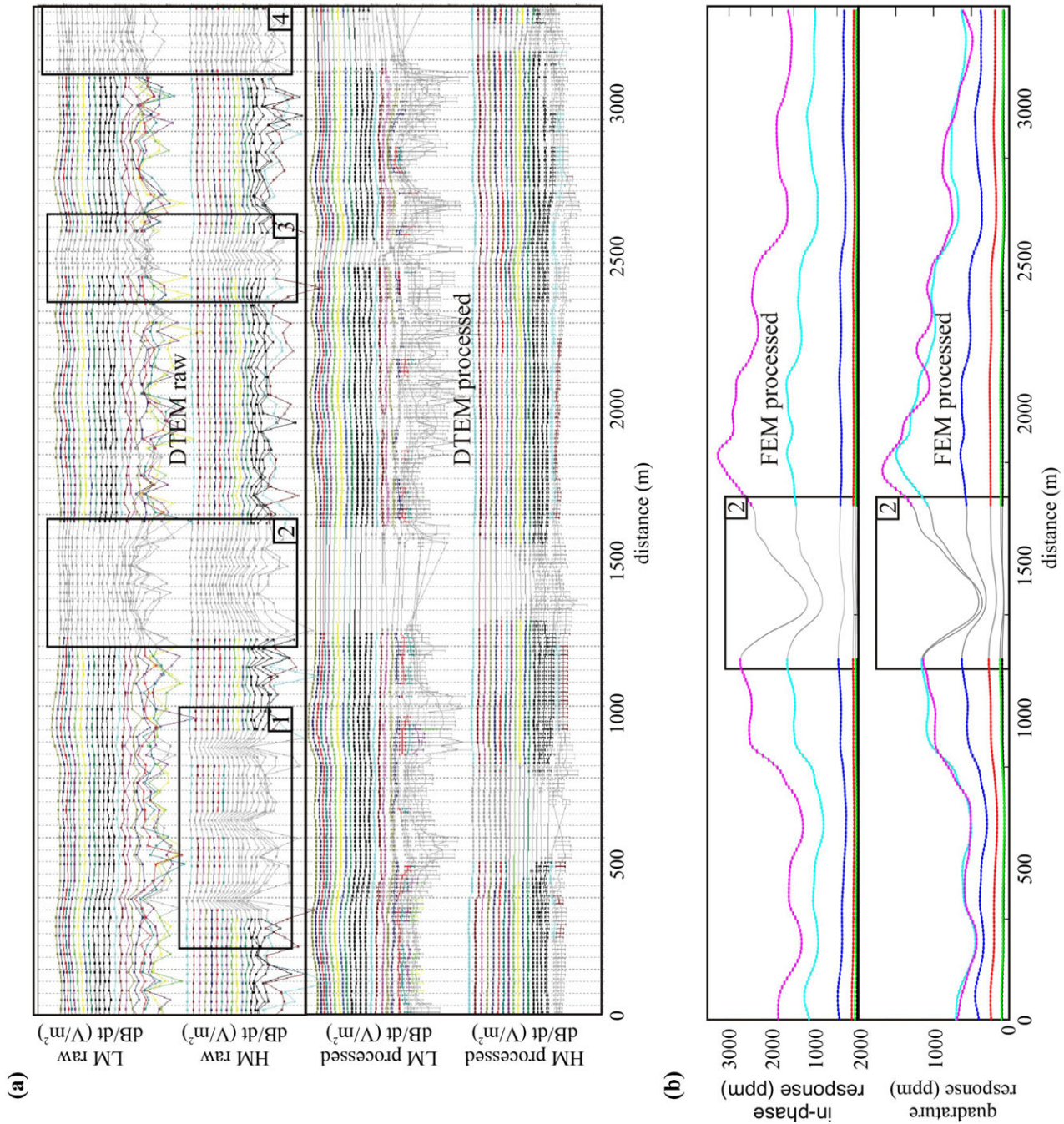


**Figure 4** Spatially collocated data segments within the Sidney block from (a) DTEM and (b) FEM systems. Each time window corresponds to roughly 3 minutes of measured data. Each curve represents a particular (a) time gate or (b) FEM systems. Average DTEM data correspond to the result of the post-processing stack (Table 3). Numbered boxes indicate where cultural noise has been identified in the data and discarded from the data set.

**Table 4** Inversion parameters of the smooth SCI. A description of the regularization parameters can be found in Auken and Christensen (2004).

	STEM	DTEM	FEM
Gates <sup>a</sup> /Frequencies used for the inversion	113 $\mu$ s to 3.2 ms	LM: 5 $\mu$ s to 221 $\mu$ s HM: 33 $\mu$ s to 4.5 ms	400 Hz to 130 kHz
Gates/Frequencies disregarded	58 $\mu$ s, 86 $\mu$ s	LM: 3 $\mu$ s, 281 $\mu$ s – 1.1 ms HM: 3 – 61 $\mu$ s, 5.7 ms, 7.1 ms	–
Nb. Of layers	20	20	20
Thickness of 1 <sup>st</sup> layer (m)	1.5	1.5	1.5
Last interface depth (m)	250.0	250.0	70.0
Starting resistivity ( $\Omega$ m)	100.0	100.0	100.0
Vertical constraint	3.0	3.0	3.0
Lateral constraint	1.35	1.35	1.35

<sup>a</sup>The zero timing is defined as the end of the ramp

particularly the deeper parts, which are poorly constrained by the data.

The vertical regularization was set quite loose (Table 4) so that vertical discontinuities in resistivity, as are expected across unconformities, are only slightly penalized by the inversion. For each data set, 20 layers were defined, with the thickness of layers increasing logarithmically with depth but remaining fixed during the inversion. Between systems, we chose to vary the depth to the last interface in order to match the relative DOI of each system. As discussed earlier, the present FEM system is expected to provide the highest near-surface resolution yet given the modest Tx moments, i.e., the smallest DOI. The STEM system, in contrast, is expected to have a large DOI given its Tx moment but the lowest near-surface resolution as its earliest time gate is beyond 100  $\mu$ s. The DTEM is expected to be closest to the FEM system in terms of near-surface resolution, with the first gate at 5  $\mu$ s after current turn-off yet closer to the STEM system in terms of DOI. Therefore the discretization of FEM models is the finest in the top 70 m, with the first layer of 1.5 m and the last interface depth at 70 m (Table 4). We chose to use the same discretization for STEM and DTEM systems, which have comparable DOIs. For both of these systems, the first layer has a thickness of 1.5 m, but the last interface depth is set to 250 m.

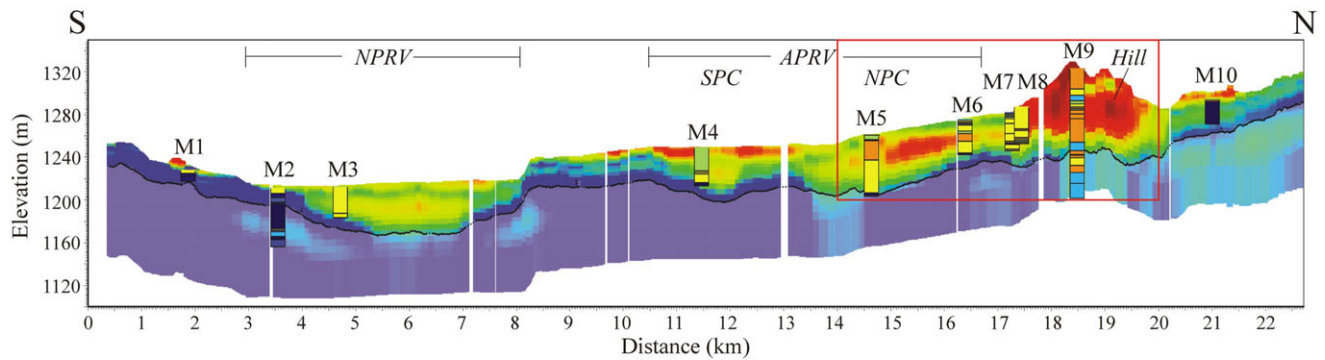
## 4 RESULTS AND DISCUSSION

The inversion models from each area are shown in parasession (with depth derived from numerous 1-D layered-earth inversions) for a single profile within the MTB (Fig. 5) and the STB (Fig. 6). All parasessions are shown on a common logarithmic resistivity colour scale and with a vertical exaggeration of 20:1. All parasessions are further referenced to a common elevation surface. The DOI is displayed as a black line within each model parasession, below which the resistivity–depth image is semi-transparent, meaning that interpretation of these parts of the model section should be carried out with caution. To permit a more detailed examination of the models in relation to borehole lithology, Fig. 7 shows an expanded view of the north and south ends of the MTB and STB, respectively.

To examine the models in map view, gridded horizontal slices were calculated at specified depths below land surface (bls) via 2-D kriging using a search radius of 600 m. The sampled and modelled semivariograms corresponding to each system are discussed later. Figures 8 and 9 show model depth slices at 10 m, 50 m, and 150 m bls for the MTB and STB, respectively. The locations of data used during the inversion (following the removal of coupled data) are superimposed upon the resistivity maps. Any region below the calculated DOI has been blanked from the depth slices. Table 5 provides a summary of the average data misfit and DOI for each system. The model response for each system fits the measured data to a data residual less than 1, the exception being the FEM data flown over the MTB. Examination of the residual distribution for this data set reveals one frequency with consistently higher data residual than the other frequencies and may be associated with a systematic bias at this frequency. The FEM device flown above STB is not exactly the same and does not present the same issue. The STEM data residual is well below 1, suggesting that the data are being overfit. This being said, overfitting of data is typically manifest in coarse or speckled models, something we do not observe in Figs. 5 and 8. Overestimated data errors may also explain the unusually low STEM residual, although we have applied an identical error estimation approach to both the STEM and DTEM systems.

While we have made every attempt to remove data coupled to infrastructure prior to inversion, we note linear features visible at 10-m depth within the STEM models and at 50-m depth within the MTB FEM models (white ellipses in Fig. 8). These features are in close proximity to powerlines and pipelines and reflect the residual effects of coupling rather than geologic structure. This highlights

## (a) FEM



## (b) STEM

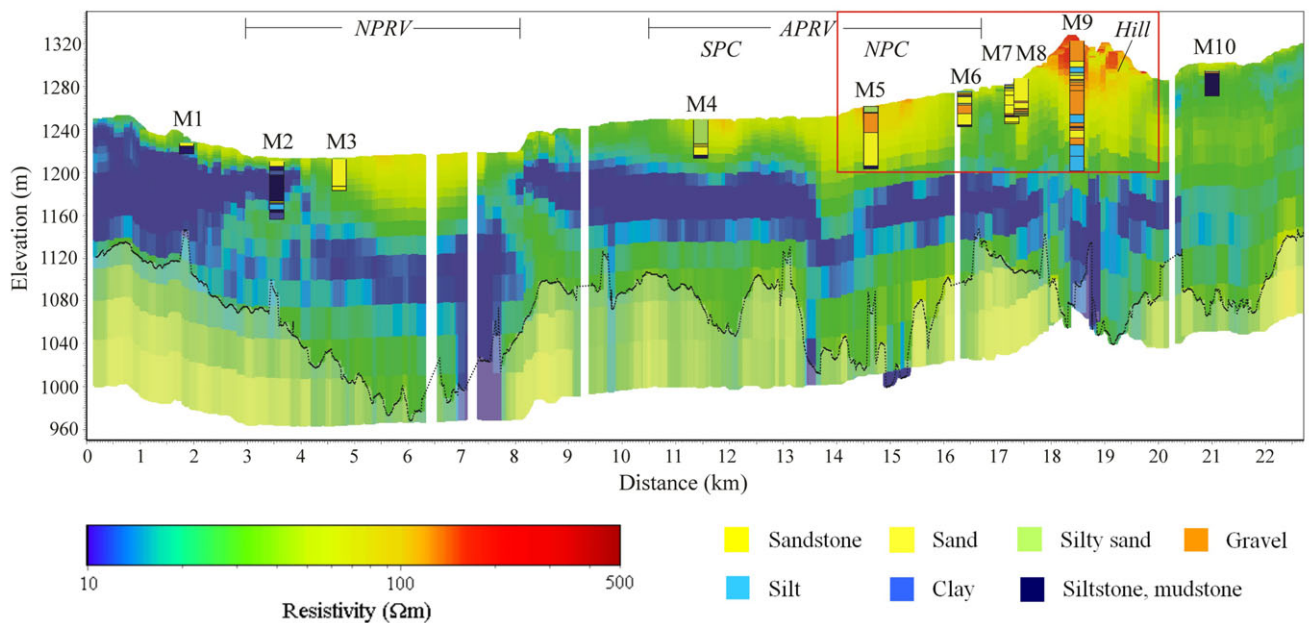


**Figure 5** Comparison of (a) FEM and (b) STEM resistivity parasectons within the Morrill block. Location of the profile is shown in Fig. 1a. Red box indicates the extent of Fig. 7a. Transparency indicates regions below the DOI, which is also shown as a dark line. Strip plots indicate borehole lithology. Boreholes M9 and M10 were located 400 m and 850 m, respectively, from the profile; all other boreholes were within 100 m of the profile. NPRV = North Platte River Valley; APRV = Ancestral Platte River Valley; NPC = north paleochannel; SPC = south paleochannel; Hill = hillside-armouring Broadwater Formation.

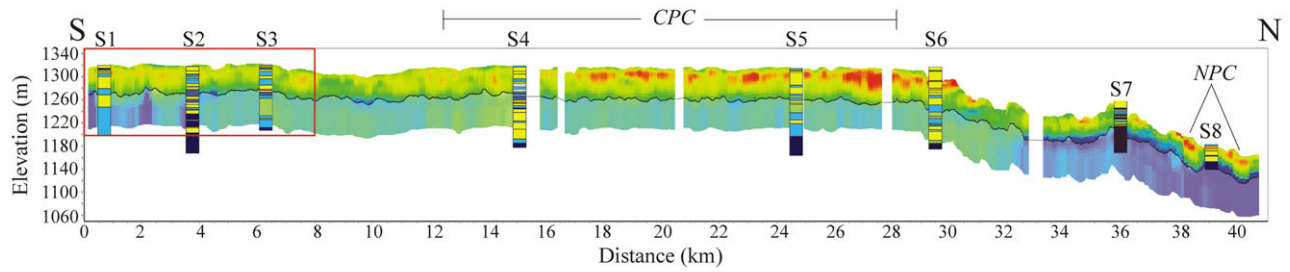
the importance of removing all coupling prior to stacking and filtering. FEM data are typically delivered after initial stacking and filtering (Table 3), which tends to smear out any coupling in the data. The user is then faced with a choice of removing large portions of the data or accepting the presence of conductive artefacts within the inversion models.

In what follows, we present a discussion of the inverted models in terms of model structure and borehole lithology (4.1), comparison to GTEM data (4.2), spatial variability and model resolution (4.3), and model intercorrelation (4.4).

#### 4.1 General model structure and borehole lithology

Within both test blocks, all systems image a generally resistive aquifer above a conductive aquitard. The depth of the aquifer–aquitard interface, hereafter referred to as the BOA, varies significantly within each test block, i.e., from the land surface to ~100-m depth in the MTB and from the land surface to ~200-m depth in the STB. We examine the various models within each test block with regard to the resolution of basic model features, the definition of the BOA, the resistivity contrast in the models, and internal aquifer stratigraphy.

## (a) FEM



## (b) DTEM

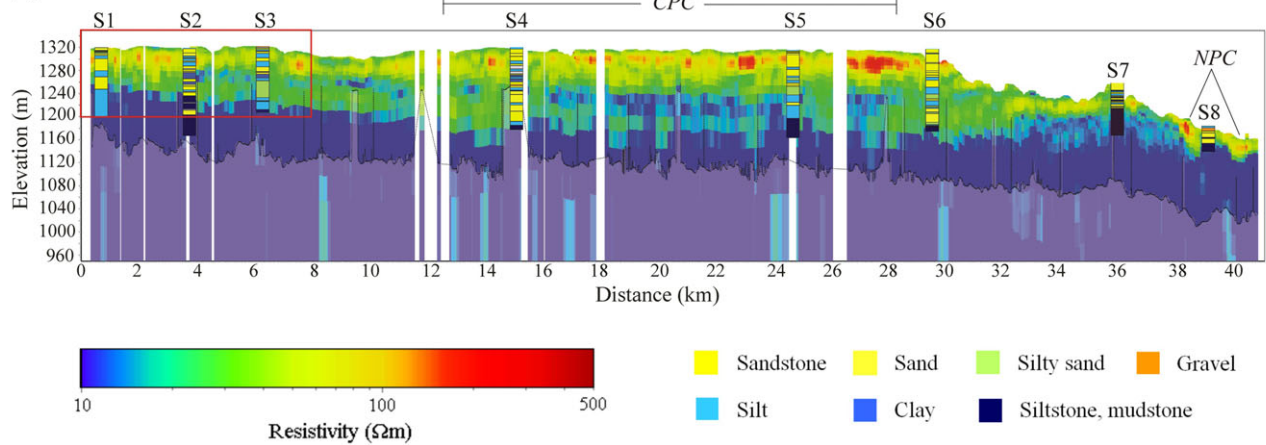


**Figure 6** Comparison of (a) FEM and (b) DTEM parassections within the Sidney block. Location of the profile is shown in Fig. 1b. Red box indicates the extent of Fig. 7b. Transparency indicates regions below the DOI, which is also shown as a dark line. Strip plots indicate borehole lithology. Boreholes S4, S6, and S8 were located 2200 m, 1400 m, and 1100 m, respectively, from the profile; all other boreholes were within 400 m of the profile. NPC = northern paleochannel system; CPC = central paleochannel system

**Table 5** Summary of data residual (sum of the squared difference between measured datum and model response at each gate/frequency normalized by data variances) and DOI. STD corresponds to standard deviation.

Area	System	Data residual		DOI (m)	
		Average	STD	Average	STD
Morrill	STEM	0.34	0.17	234.	49.0
	FEM	1.18	0.19	51.9	16.2
Sidney	FEM	0.87	0.16	64.1	9.4
	DTEM	0.62	0.34	218.	38.9

#### 4.1.1 MTB area

Within the MTB, both the FEM and STEM models recover the primary structures crossing the test block. These include the NPRV, north and south paleochannels within the ancestral Platte River Valley (APRV), and the “Hill” as designated in Figs. 5 and 8. The FEM models appear to better delineate the

geometry of these features from the surface to ~50-m depth; however, only the STEM models are able to resolve the deeper extent of these features, such as the north paleochannel and the hill. The location of the BOA is typically indicated on borehole lithology logs as a transition from sands and gravels to siltstone or mudstone. The topography of this interface, in comparison with borehole lithology, is well recovered by the FEM models but less so within the STEM model parassections. Where the BOA is shallow (e.g., borehole M1), the STEM models provide an overestimate of aquifer thickness, likely reflecting the lack of early-time data needed to constrain near-surface resistivity structure (Table 4). As compared with the FEM models, the STEM models also show less dynamic range in resistivity. The resistivity contrast between aquifer sands and gravels and the underlying siltstones and mudstones of the Brule Formation (Table 1) is noticeably less in the STEM models than in the FEM models. The top of the Brule Formation, for example, corresponds to a resistivity of 10  $\Omega\text{m}$ –15  $\Omega\text{m}$  in the FEM parassection but ranges as high as 40  $\Omega\text{m}$  in the STEM parassections (e.g., boreholes M4–M6 in Figs. 5

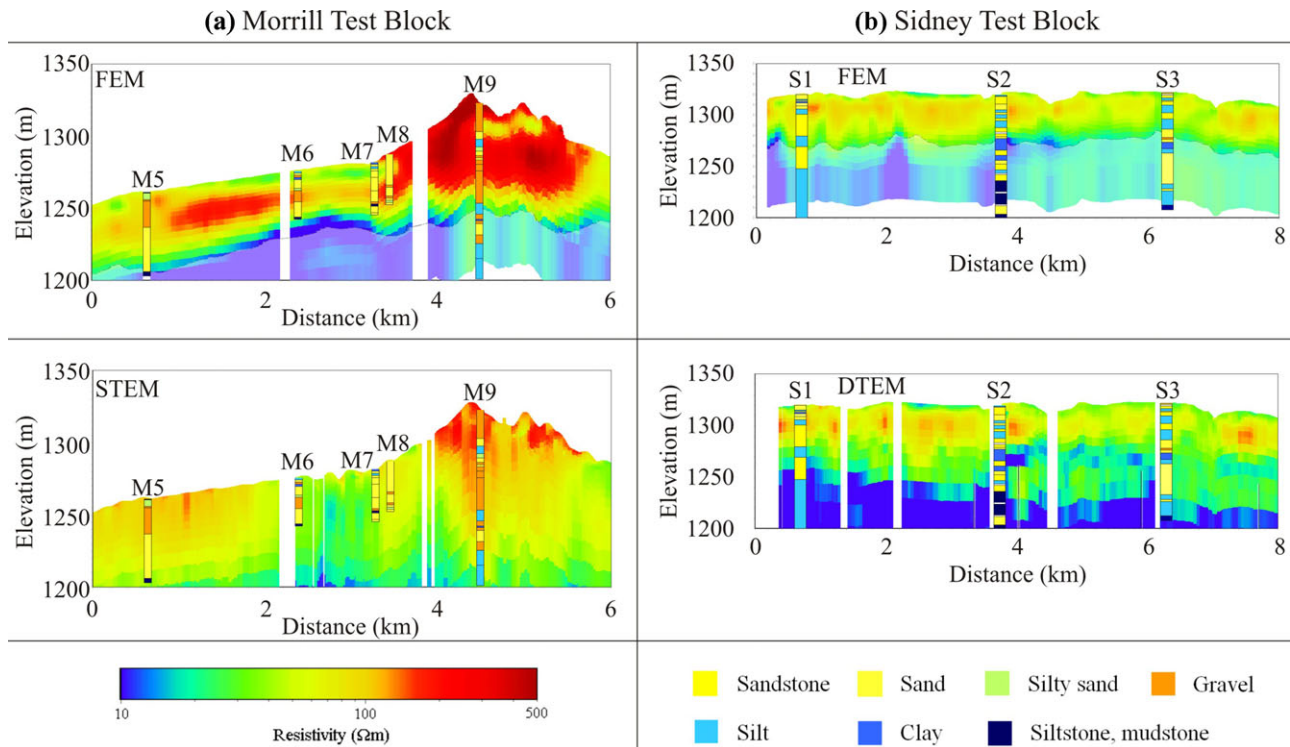


**Figure 7** Expanded view of resistivity parassections in Figs. 5 and 6. (a) Comparison of FEM and STEM models within the MTB. (b) Comparison of FEM and DTEM models within the STB. Strip plots indicate borehole lithology. Boreholes M5–M9 and S1–S3 correspond to the white circles closest to the profile in Fig. 1.

and 7). Borehole resistivity logs within the area (not shown) are more consistent with the resistivity values recovered in the FEM model parassections, as are local and regional GTEM models (see section 4.2).

The STEM and FEM models differ as well with regard to imaging internal aquifer stratigraphy. The FEM model reveals layering within the NPRV that is supported by borehole lithology; such layering is not evident within the STEM models, which recover an average aquifer resistivity, again attributed to limited early-time data. The models also differ in their imaging of coarse-grained sand and gravel lenses within the north and south paleochannels. The FEM models reveal distinct pockets of increased resistivity, the boundaries of which agree well with borehole lithology (e.g., boreholes M5 and M6 in Fig. 7). The STEM models, in contrast, image a more subtle and diffuse resistivity increase in these regions. At the north end of the MTB, a thick resistive zone (the Hill) is imaged in both models, consistent with a thick package of sand and gravel identified in borehole M9 (Fig. 7). At a finer scale, the FEM models image a narrow conductive zone at and to the north of M9 that correlates with a silt layer in the borehole; the STEM models

beneath M9 do not resolve this conductive layer. Finally, 2 km–3 km north of the Hill, a few-metre-thick veneer of sand and gravel is reflected in borehole lithology (M10) and surface geology (<http://snr.unl.edu/data>). This lithologic boundary is reflected in the FEM models but not by the STEM models.

#### 4.1.2 STB area

The STB models image a thick and highly variable aquifer that thins considerably to the north (Figs. 6 and 9). Defining a BOA and subdividing the Tertiary stratigraphy within the STB is problematic; a silt and clay layer is recorded in lithologic logs at a depth of 50 m–100 m, particularly in the centre of the STB, and may be part of the Ogallala Group or the Brule Formation. This layer, which we term the local confining unit, is typically separated from deeper silt, siltstone, and mudstone (the regional confining unit) by up to 40 m of sand (e.g., boreholes S3, S4, and S6). Both the local and regional confining units are evident within the DTEM resistivity models, the former appearing to be laterally discontinuous. Given the more limited DOI of the FEM system, neither the local nor

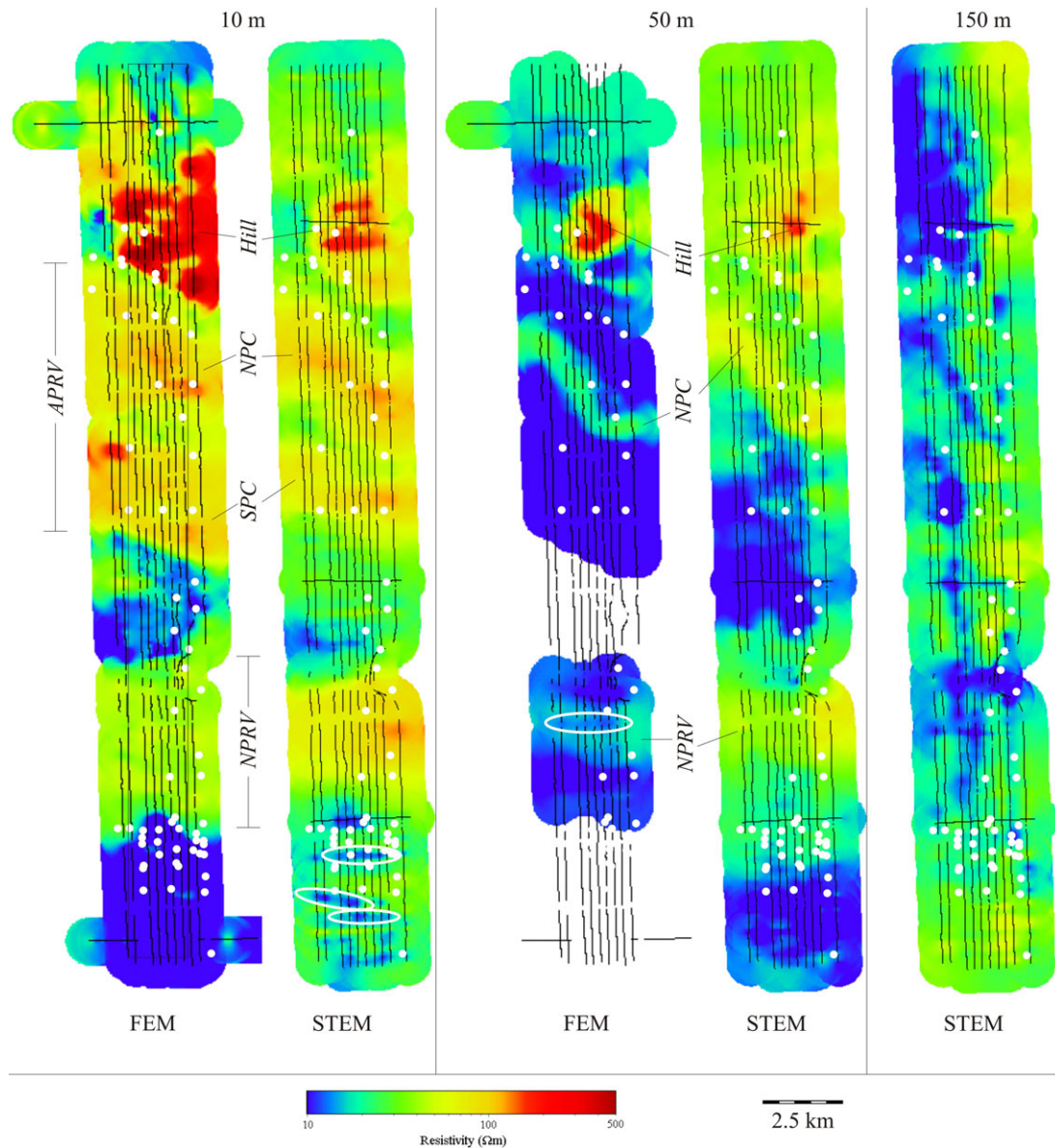


**Figure 8** Comparison of kriged model depth slices within the MTB. Models are shown at 10 m, 50 m, and 150 m bls. All depth slices are shown on a common colour scale, and regions below the calculated DOI are blanked out. The distribution of data used in the inversion is indicated in black. White circles indicate boreholes within the survey area. Labelled features are discussed in the text. Model structure within white ellipses reflects coupling to man-made infrastructure. Labels are as in Fig. 5.

the regional confining units are imaged by this system within the central portion of the STB. At the north end of the STB, where the regional confining unit comes to within 40 m of the surface, the FEM models accurately image this boundary (e.g., boreholes S7 and S8).

The DTEM models show the greatest DOI, on average, sensing 100 m deeper than the FEM models. None of the systems, however, have the penetration required to image the

top of the highly conductive (5- $\Omega\text{m}$ ) Pierre shale at  $\sim 1000$  m asl, an admittedly difficult target to image beneath  $\sim 200$  m of 10  $\Omega\text{m}$ –15  $\Omega\text{m}$  Brule Formation (Table 1).

Small differences are observed between the two models in the detailed structure above the regional confining unit. However, the overall similarity of the FEM and DTEM models in the near surface, as well as their consistency with borehole lithology (e.g., a thin silt layer at the surface in boreholes

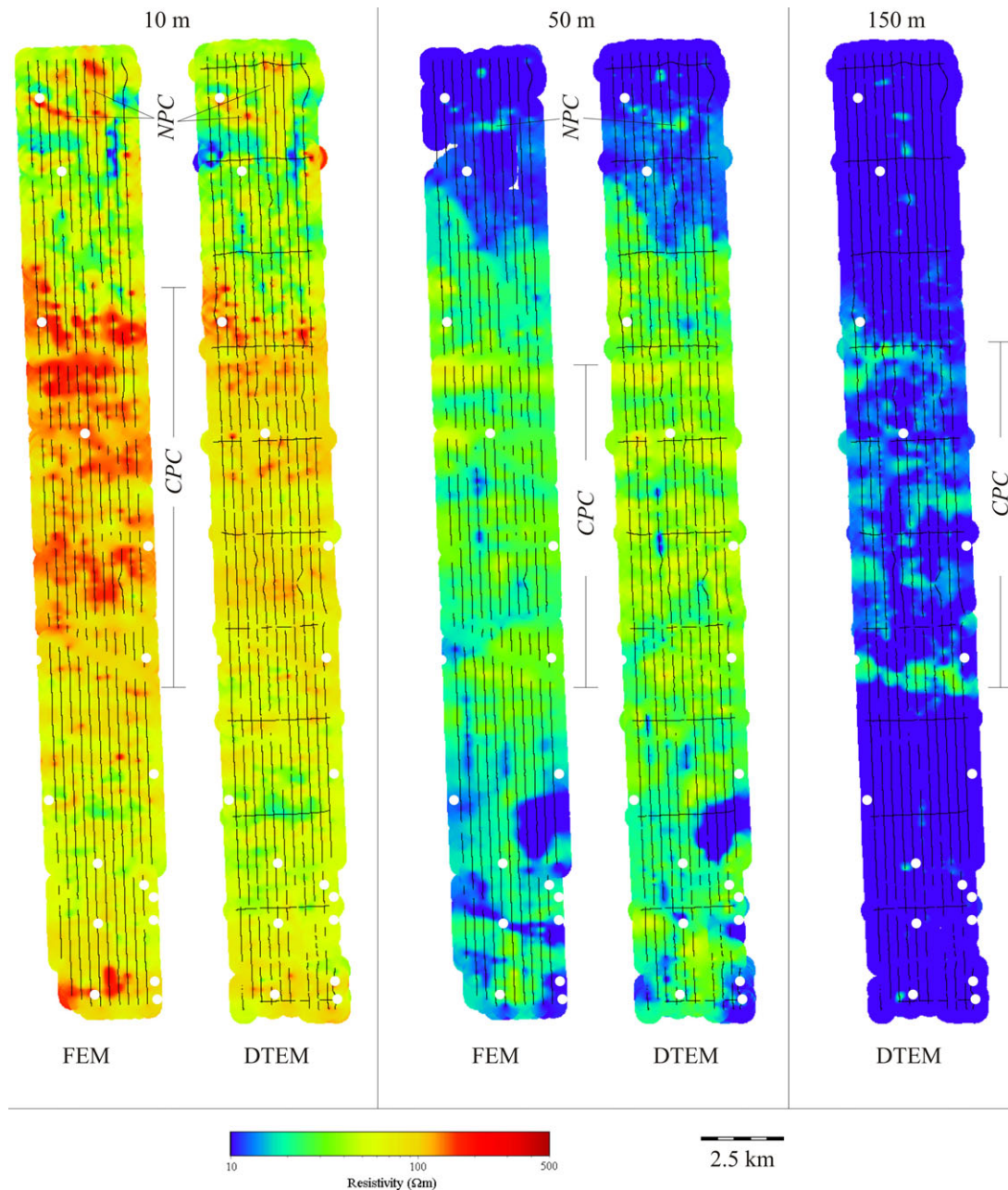


**Figure 9** Comparison of kriged model depth slices within the STB. Models are shown at 10 m, 50 m, and 150 m bls. All depth slices are shown on a common colour scale, and regions below the calculated DOI are blanked out. The distribution of data used in the inversion is indicated in black. White circles indicate boreholes within the survey area. Labelled features are discussed in the text. Labels are as in Fig. 5

S4 and S5) and with GTEM models (section 4.2), shows evidence for the consistency of the results provided by these two systems.

Primary structural features within the STB (Figs. 6 and 9) include a shallow paleochannel system at the northern end of the STB (NPC) and a broad and deep paleochannel system

within the central STB (CPC). The former consists of a series of narrow well-defined paleochannels, whereas the latter consists of a broad 15-km- to 20-km-wide paleovalley, similar in scale to the modern-day NPRV.

The northern paleochannel system is imaged as a pair of resistive zones sub-parallel to the NPRV and incised into the

conductive Brule Formation to ~40-m depth. These east–west paleochannels appear connected to each other via a north–south trending paleochannel that may continue beyond the northern edge of the STB. The geometry of this paleochannel system, particularly its lower extent, is well defined by both systems (Fig. 6, either side of borehole S8).

The CPC system is a broad valley punctuated by deep well-defined paleochannels at its northern and southern edges (Figs. 6 and 9). This feature is imaged as a disruption and depression on the top of the siltstones and mudstones. The sand, silt, and gravel that fill this depression can be traced to depths in excess of 200 m. The geometry and complexity of this paleochannel system suggest that it formed as a braided river system heavily laden with sediments. The FEM model and, to a lesser extent, the DTEM model indicate the extent and geometry of the paleochannel system at depths as shallow as 10 m. By 50-m depth, both systems resolve the outer edges of the system as a subtle east–west trending increase in resistivity relative to the surrounding area. The greatest contrast is seen at 150-m depth (Fig. 9), where the DTEM models delineate the edges of the system incised within the regional confining unit, as well as interpreted sand and gravel bars within the centre. The FEM system is, on the other hand, unable to image the deep portion of this paleochannel system.

## 4.2 Ground data comparison

Comparison of the AEM data to GTEM data (Fig. 10) permits an investigation of model consistency, near-surface resolution, and DOI using parameterized inversion models that are free from the effects of regularization inherent to the SCI approach. For each of the GTEM soundings (white squares in Fig. 1), we extracted the closest AEM sounding from each data set and inverted the data using the system parameters described in Tables 2 and 3. Data errors were assigned as discussed in section 3.3. Each AEM sounding was inverted for a suite of models in which the number of layers varied from two to six. The best minimum-layer inversion model was chosen from this model suite as the model with the fewest number of layers required to fit the measured data both visually and statistically (as measured by a reduced  $\chi^2$  goodness-of-fit statistic). In comparison with this “best” model, models with more layers show no significant reduction in  $\chi^2$  or improvement in visual fit to the measured data. Of all the GTEM soundings, we display the two soundings from each test block (Fig. 10) where the following criteria are best satisfied on average among all systems: (i) lowest system altitude; (ii) smallest

distance between ground and AEM soundings; (iii) maximum DOI; and (iv) maximum distance from identified couplings.

In addition to the model–space comparison, we calculate the synthetic forward response of each minimum-layer model for an idealized ground system TEM recording between 10  $\mu$ s and 10 ms after current turn-off. The plots in Fig. 10 permit an examination of how system bandwidth, DOI, and system bias are reflected both in the model and data spaces.

### 4.2.1 MTB area

At ground soundings NP1 and NP3, the STEM and FEM models show similar resistivity–depth trends to the corresponding GTEM models. At NP1, the models agree quite well within the upper 60 m, though both AEM models place the first layer interface about 5 m above the corresponding GTEM model. Below 60 m, the limited DOI of the RESOLVE model prohibits further comparison. In the deeper section, both the GTEM and airborne STEM models image a 20-m- to 30-m-thick resistor; however, the top and bottom of this resistive layer are shifted downward by ~20 m and ~10 m, respectively, in the STEM model. Finally, the resistivity of the deepest conductive layer differs by more than a factor of 2 between the GTEM and STEM systems, a difference that is distinguishable in the synthetic ground response.

Greater discrepancy is seen at NP3, where a general increase in conductivity with depth is observed. The STEM model is significantly more resistive than the GTEM model from the surface to 150-m depth. The last layer interface, corresponding to a drop in resistivity of nearly an order of magnitude, is ~40 m deeper in the STEM model than in the GTEM model. This is reflected in the synthetic ground response as well, where STEM apparent resistivities are uniformly higher than for the other systems. Within its DOI, the FEM model has very similar resistivities compared with the GTEM model; however, the first layer interface is shifted down ~15 m relative to the ground model. The consistency of this particular interface between the STEM and FEM models, based upon data 100 m from NP3, suggests that the discrepancy may be associated with lateral variability in subsurface resistivity. The synthetic ground response of the FEM model diverges from the ground model response at times greater than 1 ms due to the large difference in DOI between the FEM and GTEM systems.

At both sites, the synthetic STEM apparent resistivities are higher than for the synthetic GTEM data at early and mid-times but descend steeply, crossing the GTEM apparent resistivity curves at late times. This behaviour may indicate a systematic bias in the STEM data.

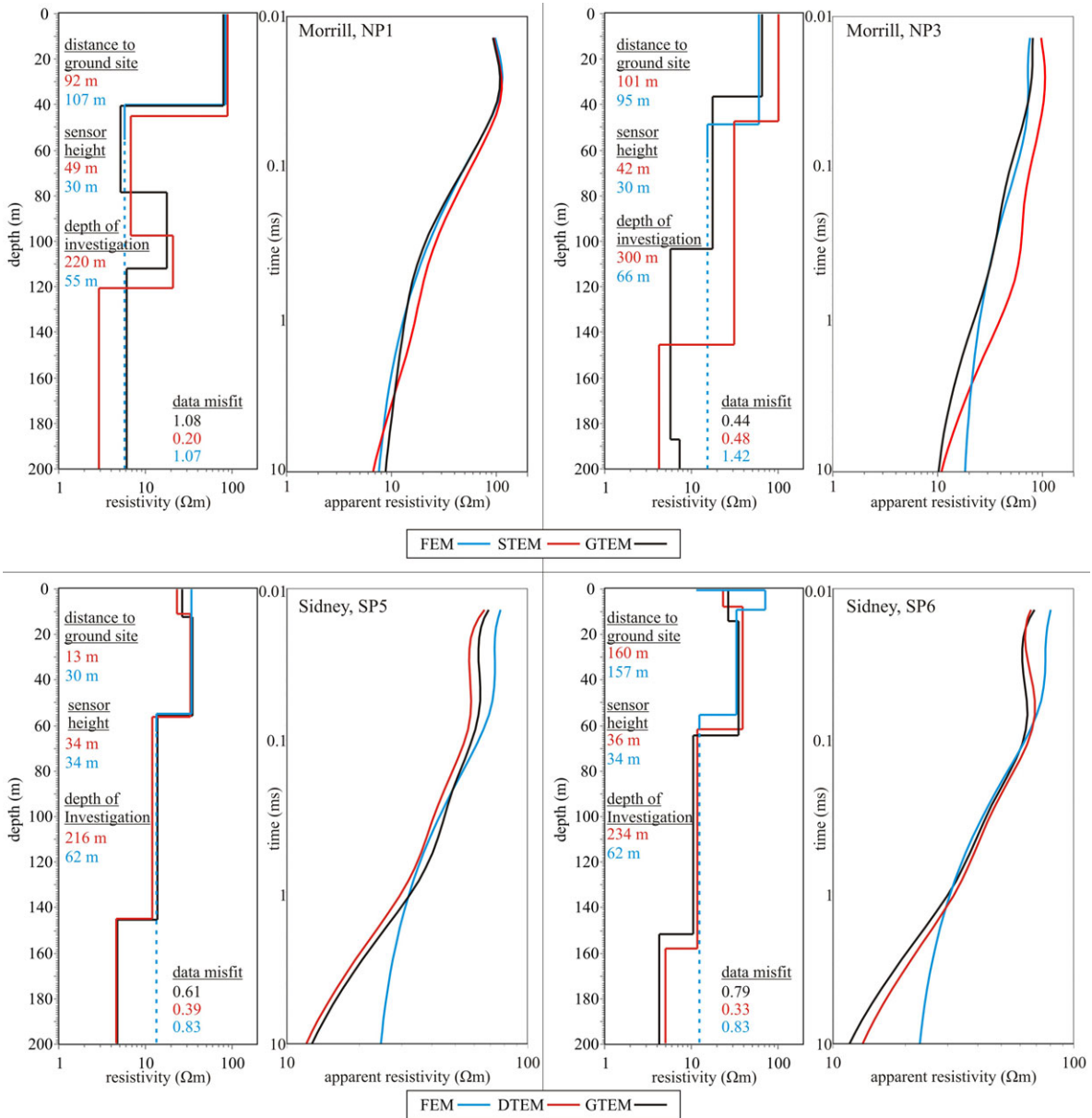


**Figure 10** Model-space and data-space comparisons of AEM and ground data. Model-space comparison shows best fit minimum-layer inversion models from each AEM system compared with a ground-based TEM model. The distance between each AEM sounding and the ground site, the altitude of each AEM system, the DOI associated with each model, and the data residual are indicated. Data-space comparison shows the forward response of each inversion model for an idealized GTEM system recording from 10  $\mu\text{s}$  to 10 ms after current turn-off. Dashed line corresponds to the part of the resistivity model located below the DOI. Site locations are shown in Fig. 1.

#### 4.2.2 STB area

At soundings SP5 and SP6, a close correlation is seen between the GTEM and DTEM models from 15 m to over 200 m bls. The FEM models have a much smaller DOI but are in lock step with the GTEM model from 15 m to 50 m. The different late-time ( $> 1$  ms) synthetic response for the FEM system relative

to the other systems is due to the limited DOI. The layer interface around 60 m at sounding SP6 shows about 10-m discrepancy between the FEM and GTEM models; however, the resistivities above and below this interface agree closely.

The near surface shows small differences between the ground and AEM models. At SP5, the GTEM, DTEM, and FEM systems are similar in both the model and data spaces.

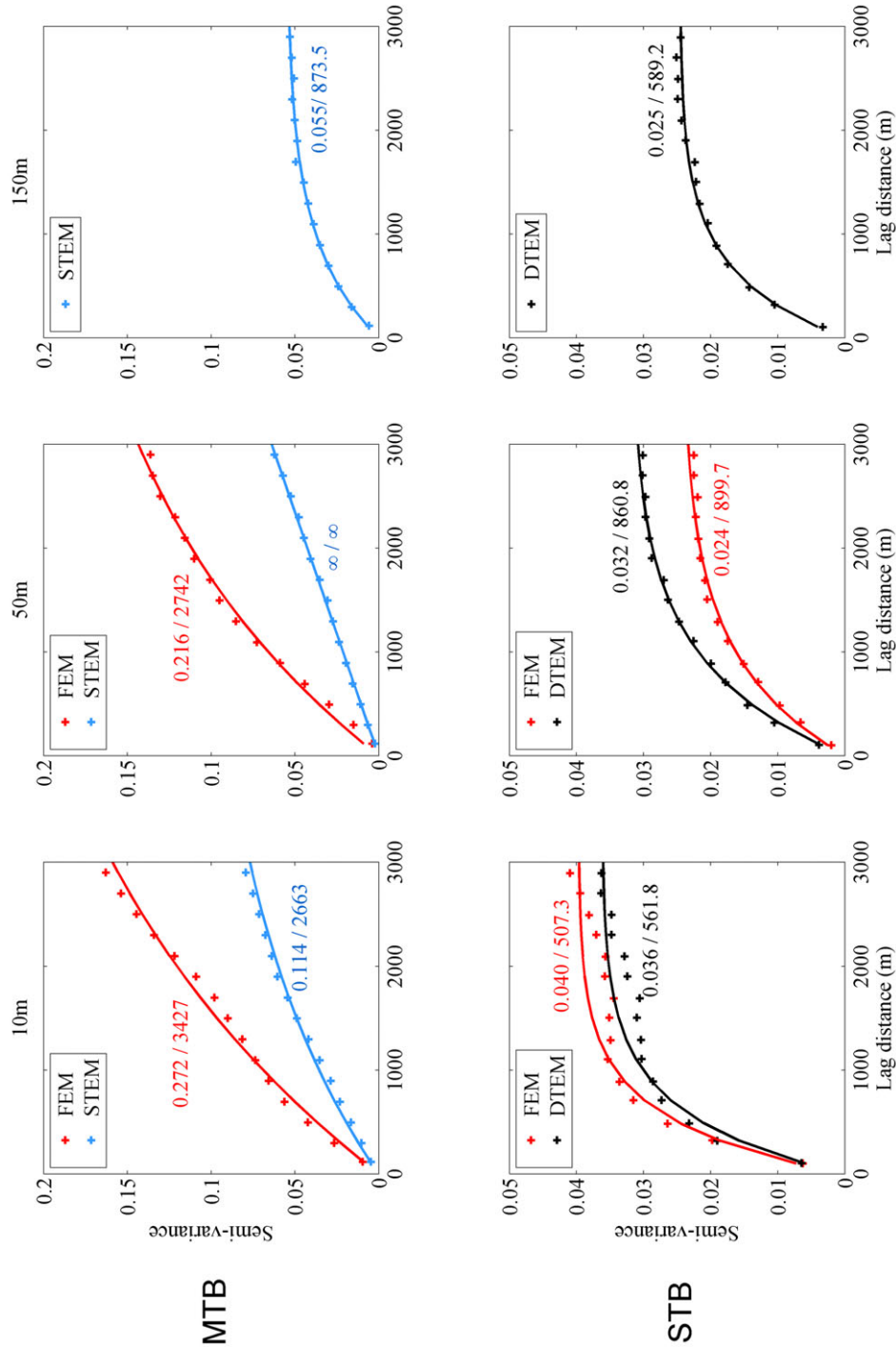


**Figure 11** Experimental and modelled semivariograms for resistivity model at 10 m, 50 m, and 150 m bls for the Morrill (MTB) and Sidney (STB) test blocks. The solid lines correspond to the modelled semivariograms using an exponential function. The sill (dimensionless) and range (metres) for each modelled semivariogram are annotated next to each curve. As the FEM system has a more limited DOI, no resistivity values are available at 150-m depth. Note that the vertical scale is different between the two test blocks, reflecting greater spatial continuity in the STB.

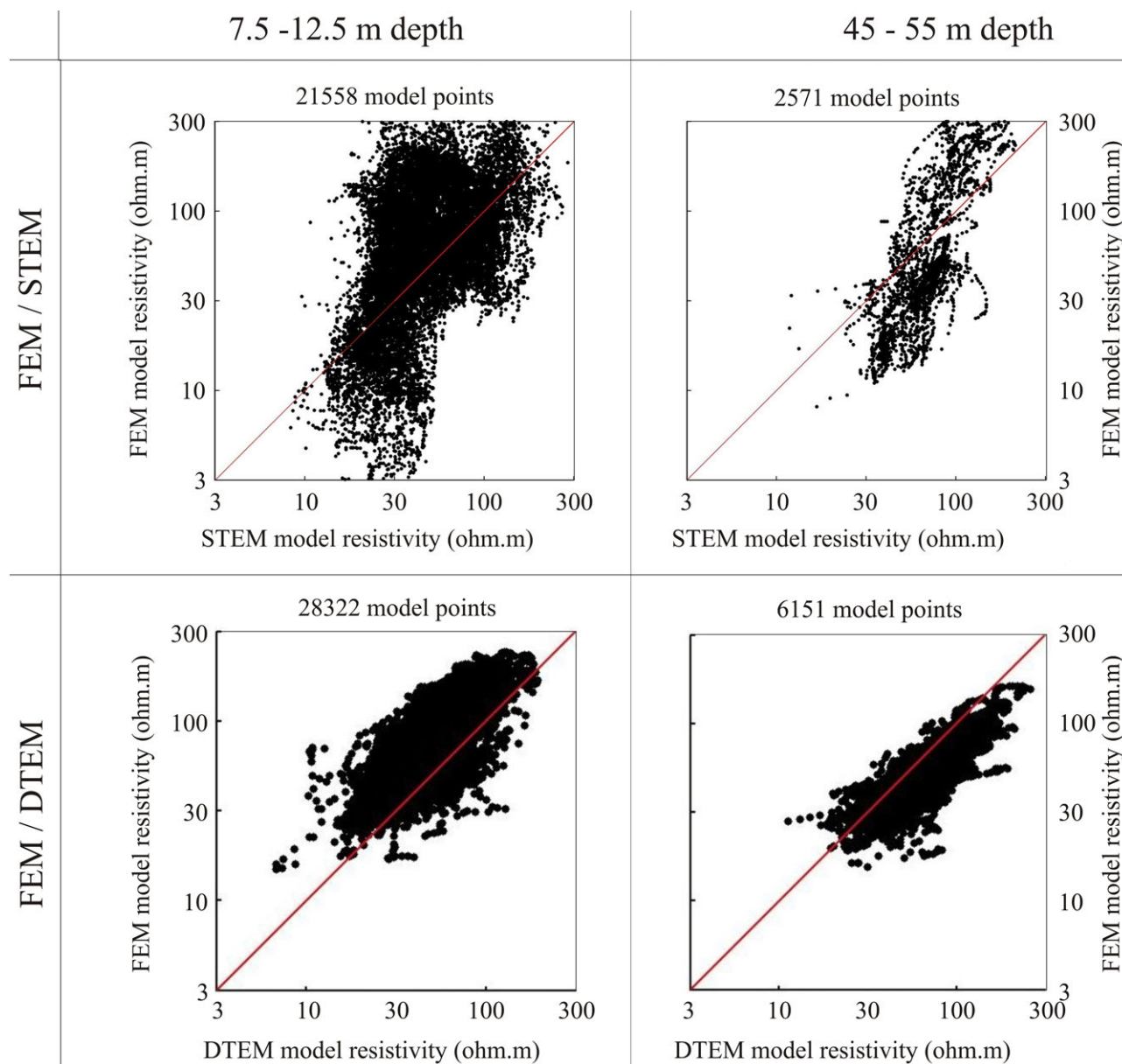


**Figure 12** Model cross-plots for each pair of systems within specified depth ranges. Cross-plots between any two systems include all collocated model points within the test block that fall above the calculated DOI. Deviation from the unit slope line (red) reflects systematic variation between the resistivity models in the given depth range.

At SP6, a split is observed between GTEM and DTEM models, which suggest a more conductive near surface, and FEM models, which suggest a more resistive near surface. These results highlight the variation in response of different systems within the upper 10 m–20 m, which may be the result of near-surface spatial variability. Alternatively, such variations may reflect inaccuracy in system calibration and timing.

### 4.3 Spatial variability and model resolution

The depth slices shown in Figs. 8 and 9 were created by kriging (Stein 1999) log resistivity values from the individual inverted models. This procedure involves calculating and modelling semivariograms at various depths for each system. First, experimental semivariograms are estimated from the geolocated resistivity models. These semivariograms illustrate the spatial

variability in model resistivity as a function of distance. In a second step, theoretical semivariograms are estimated to fit the experimental ones. This step consists in the estimation of the range and sill parameters for a basis function (here, an exponential). The range (in metres) corresponds to the distance at which a plateau is reached in the semivariogram curve. At distances greater than the range, data points are considered to have no spatial correlation. The range can thus be interpreted as the size of the largest structures that can be observed in the data set. The sill corresponds to the amplitude of the plateau and, because of the absence of correlation between data points, to the variance of the data set. Semivariogram models with different range values indicate different spatial coherence lengths, whereas models with different sill values reflect differing resistivity ranges, with a larger sill value indicating a larger dynamic range in resistivity. We note that sill values for all of the semivariogram models, regardless of which system they are derived from, are smaller than those of the unknown true earth model. This reflects the reduction in variation of the estimated model parameters inherent to any smoothing-regularized inversion (Day-Lewis and Lane 2004; Constable, Parker, and Constable 1987). In comparing semivariograms for models derived from the different systems, higher sill values more closely reflect the resistivity range of the true earth model.

Figure 11 shows both experimental and modelled semivariograms at 10-m-, 50-m-, and 150-m-depth slices for each system. Modelled sill and range values are also annotated in Fig. 11.

Looking first at the MTB, we examine spatial variability for the FEM and STEM models at the 10-m- and 50-m-depth slices. The FEM model has a higher sill than the STEM model, suggesting a broader range of resistivity values within the FEM model. The resistivities in the STEM model, as observed in Figs. 5 and 8, appear more muted, particularly in the near surface. For both data sets, the ranges are quite large, i.e., between 2.5 km and 3.5 km at 10-m and 50-m depths. This reflects the broad-length scale of the NPRV and the APRV. At 150-m depth, the STEM model is primarily below the BOA and shows a distinct reduction, relative to the near surface, in both sill and range values, reflecting less resistivity variation in the conductive Brule Formation and the absence of broad channels.

Within the STB, the models from FEM and DTEM systems have similar range values at 10 m and 50 m (Fig. 11), suggesting that they are resolving structures of similar scale lengths. The sills are also very similar at 10-m depth, indicating that the two systems have comparable resolution capabilities

at this depth. At 50-m depth, the DTEM models show a slightly higher sill value compared with the FEM system. The range of the DTEM models is somewhat less at 150 m than at 50-m depth. This reflects narrow valleys incised into the conductive BOA at the base of the broad CPC (Fig. 9).

Comparing semivariograms for the MTB and STB shows systematically higher ranges and sills within the MTB, except at 150-m depth, where the sill and range are comparable (Fig. 11). The higher range in the MTB reflects the broad river valleys with resistive fill incised into the conductive Brule Formation (c.f., resistive structures in Fig. 8). While the central paleochannel within the STB is quite broad (c.f., CPC in Fig. 9), it does not exhibit nearly the resistivity contrast seen in the MTB. Furthermore, the thick section of Ogallala sediments in the STB is quite heterogeneous on short-length scales, as reflected in the smaller range values (Fig. 11). The higher sill values within the MTB primarily reflect the highly resistive gravels beneath the hill and within the APRV. Such high-resistivity gravels are less common within the STB, as can be seen in borehole lithologic logs (Fig. 7).

#### 4.4 Model correlation

As a final means of comparing the various systems, we present model cross-plots for each pair of systems at various depths (Fig. 12). For each subplot, all model points within the test block that fall within a given depth range are considered. Note that we perform this analysis at the actual sounding locations, not on the gridded model maps. Each point contained within any given subplot corresponds to a model point for both systems that is collocated in three dimensions to within 25 m laterally and 5 m in depth. Furthermore, only model points that fall within the DOI of both systems are considered.

We begin by examining model cross-plots from the MTB for the FEM and STEM systems (top plots in Fig. 12). In both the 10-m and 50-m cross-plots, significant deviation from perfect correlation (slope equal to one) is evident. The point cloud is compressed in the horizontal direction, indicating a more muted range of resistivity in the STEM model relative to the FEM model. This is consistent with both visual observation (Figs. 5, 7, and 8) and lower sill values in the semivariograms for the STEM models (Fig. 11). For the 10-m cross-plot, corresponding to the resistive aquifer, a larger point concentration is observed above the line, indicating that the STEM model is on average less resistive than the FEM model. The opposite occurs in the 50-m cross-plot, where the

conductivity below the BOA is underestimated by the STEM model.

Cross-plots from the STB (bottom plots in Fig. 12) show the correlation between FEM and DTEM systems. In both the 10-m and 50-m cross-plots, an excellent correlation (slope close to one) is observed between the models obtained from the two systems, although FEM models systematically show slightly higher (lower) resistivities at 10-m (50-m) depth relative to the DTEM models. These differences are most likely due to the different footprints and frequency content of the two systems, which do not integrate the same volume of ground with the same resolution. Since these differences appear as constant shifts over all resistivity values, they may also suggest a need for additional system calibration, at least in amplitude. Regardless, the resistivity models obtained by FEM and DTEM are quite consistent and are expected to lead a skilled interpreter to similar hydrologic and geologic conclusions.

## 5 CONCLUSIONS

The use of AEM data for hydrologic application hinges upon the recovery of accurate and unbiased resistivity models through the process of inversion. Such models are needed from the surface to depths in excess of 200 m and must accurately recover aquifer resistivity, internal aquifer stratigraphy, and spatial variations in local and regional confining units.

We examined AEM data and inverted resistivity models from three different systems (four data sets) at two test blocks within the High Plains aquifer. The test blocks, near Morrill and Sidney, Nebraska, are representative of shallow and deep alluvial aquifer systems, respectively. Both the conductive BOA and internal aquifer stratigraphy exhibit significant variability at a range of spatial scales. The data from all systems were inverted using a common framework, and each system was characterized as accurately as possible based on specifications provided by the AEM contractors. The data as modelled incorporate any calibration, bias correction, or compensation carried out by the contractors, which normally correct for systematic data errors, system drift, and primary-field removal, respectively. Some of the findings noted in this study suggest a need for further calibration, which has not been carried out.

All of the data are capable of defining the large-scale variations in the BOA as constrained by borehole lithologic logs. The FEM system, with its more limited DOI, is unable to constrain the BOA below ~60-m depth but provides some of the most reliable estimates of the BOA at shallower depths.

The STEM data, in contrast, proved less reliable in recovering shallow model structure (both the BOA and internal aquifer stratigraphy). Both DTEM and STEM models were capable of imaging variations in the BOA in excess of 150-m depth.

Among the three studied systems, FEM and DTEM show an excellent correlation at 10- and 50-m depths. At these same depths, STEM models diverge somewhat from the FEM models and exhibit a more muted range of resistivity values in comparison to the FEM models. We attribute these discrepancies to a lack of early-time data (i.e., high-frequency content) and of small inaccuracies in the calibration of the STEM system (supported by comparison with ground soundings).

The FEM system provides superior resolution of the near surface; however, the DTEM system, with its early time gates, shows comparable results at a depth of 10 m. The lack of unbiased early-time data clearly disadvantages the STEM system for mapping the near surface. The higher moment of the TEM systems is a critical point when dealing with deep targets. The choice of AEM system thus depends on the hydrogeological target in terms of depth, spatial variability, and the resistivity of aquifer and confining units.

## ACKNOWLEDGEMENTS

This study would not have been possible without the support of the various airborne contractors. Fugro Airborne Surveys flew the STB at no cost to the U.S. Geological Survey (USGS). The authors would like to specially thank Jared Abraham and Jim Cannia who have worked for many years to advance the use of AEM methods for hydrologic applications within the USGS. We thank Jonathan Rudd (formerly Aeroquest Ltd.), Greg Hodges (Fugro Airborne Surveys), Andrea Viezzoli (Aarhus Geophysics Aps), and Flemming Effersø (SkyTEM Surveys Aps) for discussion and feedback on modelling and inversion of the data. Bas Peters is thanked for early work on the modelling and inversion, which improved the understanding of the various systems. Ben Bloss is thanked for assembly and classification of the borehole data and preliminary modelling of the GTEM data. This manuscript was greatly improved thanks to reviews by Andy Kass, Michael Asten, and an anonymous reviewer. The HyGEM-project funded by the Danish Council for Strategic Research under Contract 11-116763 has also supported this project.

## Disclaimer

Any use of trade names is for descriptive purposes only and does not imply endorsement by the USGS.

## REFERENCES

- Aarhus Geophysics. 2010. Processing and inversion of SkyTEM data – area UTM 13, 73 pp.
- Abraham J.D., Cannia J.C., Bedrosian P.A., Johnson M.R., Ball L.B. and Sibray S.S. 2012. Airborne electromagnetic mapping of the base of aquifer in areas of western Nebraska. U.S. Geological Survey Scientific Investigations Report 2011–5219, 38 pp.
- Aeroquest Surveys. 2009. Report on a Helicopter-Borne AeroTEM System Electromagnetic and Magnetic Survey – North Platte and Sandhills Project 08–041, 36 pp.
- Auken E. and Christiansen A.V. 2004. Layered and laterally constrained 2D inversion of resistivity data. *Geophysics* 69, 752–761.
- Auken E., Christiansen A.V., Jacobsen B.H., Foged N. and Sørensen K.I. 2005. Piecewise 1D laterally constrained inversion of resistivity data. *Geophysical Prospecting* 53, 497–506.
- Auken E. and Nebel K. 2001. *Getting started with SiTEM and SEMDI*. Aarhus University, 21 pp.
- Balch S.J., Boyko W.P. and Paterson N.R. 2003. The AeroTEM airborne electromagnetic system. *The Leading Edge* 22, 562–566.
- Bedrosian P.A., Ball L.B. and Bloss B.R. 2014. Airborne electromagnetic data and processing within Leach Lake Basin, Fort Irwin, California. In: *Geology and Geophysics Applied to Groundwater Hydrology at Fort Irwin*, California, Chap. G (ed D.C. Buesch). U.S. Geological Survey Open File Report 2013–1024, 20 pp., <http://dx.doi.org/10.3133/ofr20131024G>.
- Brodie R. and Sambridge M. 2006. A holistic approach to inversion of frequency-domain airborne EM data. *Geophysics* 71, G301–G312.
- Brodie R.C., Green A.G. and Munday T. 2004. Constrained inversion of helicopter AEM data for mapping the Blanchetown Clay. Paper presented at the 17th ASEG meeting, Sydney, Australia, 5 pp.
- Cannia J.C., Woodward D. and Cast L.D. 2006. Cooperative Hydrology Study COHYST Hydrostratigraphic Units and Aquifer Characterization Report, 126 pp.
- Christiansen A.V. and Auken E. 2012. A global measure for depth of investigation. *Geophysics* 77, WB171–WB177.
- Christiansen A.V., Auken E. and Viezzoli A. 2011. Quantification of modeling errors in airborne TEM caused by inaccurate system description. *Geophysics* 76, F43–F52.
- Constable S.C., Parker R.L. and Constable C.G. 1987. Occam's inversion: A practical algorithm for generating smooth models from electromagnetic sounding data. *Geophysics* 52, 289–300.
- Cunio E. 2009. Comparison of ground TEM and VTEM responses over kimberlites in the Kalahari of Botswana. Paper presented at the 20th ASEG meeting, Adelaide, Australia, 6 pp.
- Davis L.J. and Groom R.W. 2010. A comparison of airborne and ground electromagnetic data near the Grand Canyon, 45 pp.
- Day-Lewis F.D. and Lane J.W. 2004. Assessing the resolution-dependent utility of tomograms for geostatistics. *Geophysical Research Letters* 31, doi:10.1029/2004GL019617.
- Deszcz-Pan M., Fitterman D.V. and Labson V.F. 1998. Reduction of inversion errors in helicopter EM data using auxiliary information. *Exploration Geophysics* 29, 142–146.
- Dickinson J.E., Pool D.R., Groom R.W. and Davis L.J. 2010. Inference of lithologic distributions in an alluvial aquifer using airborne transient electromagnetic surveys. *Geophysics* 75, WA149–WA161.
- Diffendal R.F. 1991. Geologic map showing configuration of the bedrock surface, North Platte 1 degree by 2 degrees Quadrangle, Nebraska. U.S. Geological Survey Miscellaneous Investigations Series Map I-2277.
- Finn C.A., Deszcz-Pan M. and Bedrosian P.A. 2012. Helicopter electromagnetic data map ice thickness at Mount Adams and Mount Baker, Washington, USA. *Journal of Glaciology* 58, 1433–1443, doi: 10.3189/2012JoG11J098.
- Fischer B.C., Kollasch K.M. and McGuire V.L. 2000. Digital map of saturated thickness in the High Plains Aquifer in Parts of Colorado, Kansas, Nebraska, New Mexico, Oklahoma, South Dakota, Texas, and Wyoming, 1996 to 1997. U.S. Geological Survey Open File Report 2000–0300.
- Foged N., Auken E., Christiansen A.V. and Sørensen K.I. 2013. Test-site calibration and validation of airborne and ground-based TEM systems. *Geophysics* 78, E95–E106.
- Fugro Airborne Surveys. 2008. Resolve survey for North Platte Resource District – North Platte River, Lodgepole Creek, and Sidney Draw areas, Western Nebraska. 8035, 92 pp.
- Fugro Airborne Surveys. 2009. Resolve survey for Sidney test area, Sidney, Nebraska. 09018, 68 pp.
- Green A., Brodie R. and Munday T. 2004. Interpretation of helicopter AEM data from the Riverland area, SA. Paper presented at the 17th ASEG meeting, Sydney, Australia, 4 pp.
- Gutentag E.D., Heimes F.J., Krothe N.C., Luckey R.R. and Weeks J.B. 1984. Geohydrology of the High Plains Aquifer in parts of Colorado, Kansas, Nebraska, New Mexico, Oklahoma, South Dakota, Texas, and Wyoming. U.S. Geological Survey Professional Paper 1400-B, 63 pp.
- Hobza C.M., Bedrosian P.A. and Bloss B.R. 2012. Hydrostratigraphic interpretation of test-hole and surface geophysical data, Elkhorn and Loup River Basins, Nebraska, 2008 to 2011. U.S. Geological Survey Open File Report 2012–1227, 95 pp.
- Hodges G. and Beattie D. 2007. Comparison of HeliGeoTEM II and Dighem V over the Maimon massive sulphide deposit. Paper presented at the 10th SAGA meeting, Wild Coast, South Africa, 4 pp.
- Ley-Cooper Y. and Macnae J. 2007. Amplitude and phase correction of helicopter EM data. *Geophysics* 72, F119–F126.
- McGuire V.L., Lund K.D. and Densmore B.K. 2012. Saturated thickness and water in storage in the High Plains Aquifer, 2009, and water-level changes and changes in water in storage in the High Plains Aquifer, 1980 to 1995, 1995 to 2000, 2000 to 2005, and 2005 to 2009. U.S. Geological Survey Scientific Investigations Report 2012–5177, 28 pp.
- Minsley B.J., Smith B.D., Hammack R., Sams J.I. and Veloski G. 2012. Calibration and filtering strategies for frequency domain electromagnetic data. *Journal of Applied Geophysics* 80, 56–66.
- Nebraska Oil and Gas Conservation Commission. Well data including formation tops. Available from: <http://www.nogcc.ne.gov/NOGCCPublications.aspx> (Accessed 3 October 2014).
- Podgorski J., Auken E., Schamper C., Christiansen A.V., Kalscheuer T. and Green A.G. 2013. Processing and inversion of commercial helicopter time-domain electromagnetic data for environmental as-

- assessments and geological and hydrological mapping. *Geophysics* 78, E149–E159.
- Reid J.E. and Vrbancich J. 2004. A comparison of the inductive-limit footprints of airborne electromagnetic configurations. *Geophysics* 69, 1229–1239.
- Schamper C., Auken E. and Sørensen K.I. 2014. Coil response inversion for very early time modeling of helicopter-borne time-domain EM data and mapping of near-surface geological layers. *Geophysical Prospecting* 62, 658–674.
- SkyTEM Surveys Aps. 2010. SkyTEM Survey: Nebraska, USA Data Report, 42 pp.
- Smith B.D., Abraham J.D., Cannia J.C. and Hill P. 2009. Helicopter electromagnetic and magnetic geophysical survey data for portions of the North Platte River and Lodgepole Creek, Nebraska, June 2008. U.S. Geological Survey Open File Report 2009–1110, 34 pp.
- Smith B.D., Abraham J.D., Cannia J.C., Minsley B.J., Deszcz-Pan M. and Ball L.B. 2010. Helicopter electromagnetic and magnetic geophysical survey data, portions of the North Platte and South Platte Natural Resources Districts, western Nebraska, May 2009. U.S. Geological Survey Open File Report 2010–1259, 33 pp.
- Smith R.S., Annan A.P. and McGowan P.D. 2001. A comparison of data from airborne, semi-airborne, and ground electromagnetic systems. *Geophysics* 66, 1379–1386.
- Smith R.S., Koch R., Hodges G. and Lemieux J. 2011. A comparison of airborne electromagnetic data with ground resistivity data over the Midwest deposit in the Athabasca basin. *Near Surface Geophysics* 9, 319–330.
- Sørensen K.I. and Auken E. 2004. SkyTEM—A new high-resolution helicopter transient electromagnetic system. *Exploration Geophysics* 35, 191–199.
- Steele G.V., Sibray S.S. and Quandt K.A. 2007. Evaluation of ground water near Sidney, western Nebraska, 2004–05. U.S. Geological Survey Scientific Investigations Report 2007–5086, 54 pp.
- Stein M.L. 1999. *Interpolation of Spatial Data – Some Theory for Kriging*. Springer. ISBN: 9781461214946.
- Steuer A., Siemon B. and Auken E. 2009. A comparison of helicopter-borne electromagnetics in frequency- and time-domain at the Cuxhaven valley in Northern Germany. *Journal of Applied Geophysics* 67, 194–205.
- Swinehart J.B. and Diffendal R.F. 1998. Geology. In: *An Atlas of the Sand Hills* (eds A.S. Bleed and C. Flowerday), pp. 29–42. University of Nebraska-Lincoln. ISBN: 9781561610020.
- Swinehart J.B., Souders V.L., DeGraw H.M. and Diffendal R.F. 1985. Cenozoic paleogeography of western Nebraska. In: *Cenozoic Paleogeography of West-Central United States* (eds R.M. Flores and S.S. Kaplan), pp. 209–229. Society of Economic Paleontologists and Mineralogists. ISBN: 9789990706086.
- University of Nebraska-Lincoln Conservation and Survey Division. Test hole database. Available from: <http://snr.unl.edu/data/geologysoils/NebraskaTestHole/NebraskaTestHoleIntro.asp> (Accessed 3 October 2013).
- Verstraeten I.M., Steele G.V., Cannia J.C., Hitch D.E., Scriptor K.G., Bohlke J.K. *et al.* 2001. Interaction of surface water and ground water in the Dutch Flats area, western Nebraska, 1995–99. U.S. Geological Survey Water Investigations Report 2001–4070, 56 pp.
- Viezzoli A., Christiansen A.V., Auken E. and Sørensen K. 2008. Quasi-3D modeling of airborne TEM data by spatially constrained inversion. *Geophysics* 73, F105–F113.
- Viezzoli A., Jørgensen F. and Sørensen C. 2013. Flawed processing of airborne EM data affecting hydrogeological interpretation. *Groundwater* 51, 191–202.
- Viezzoli A., Munday T. and Cooper Y.L. 2012. Airborne electromagnetics for groundwater salinity mapping: case studies of coastal and inland salinisation from around the world. *Bollettino di Geofisica Teorica ed Applicata* 53, 581–600.